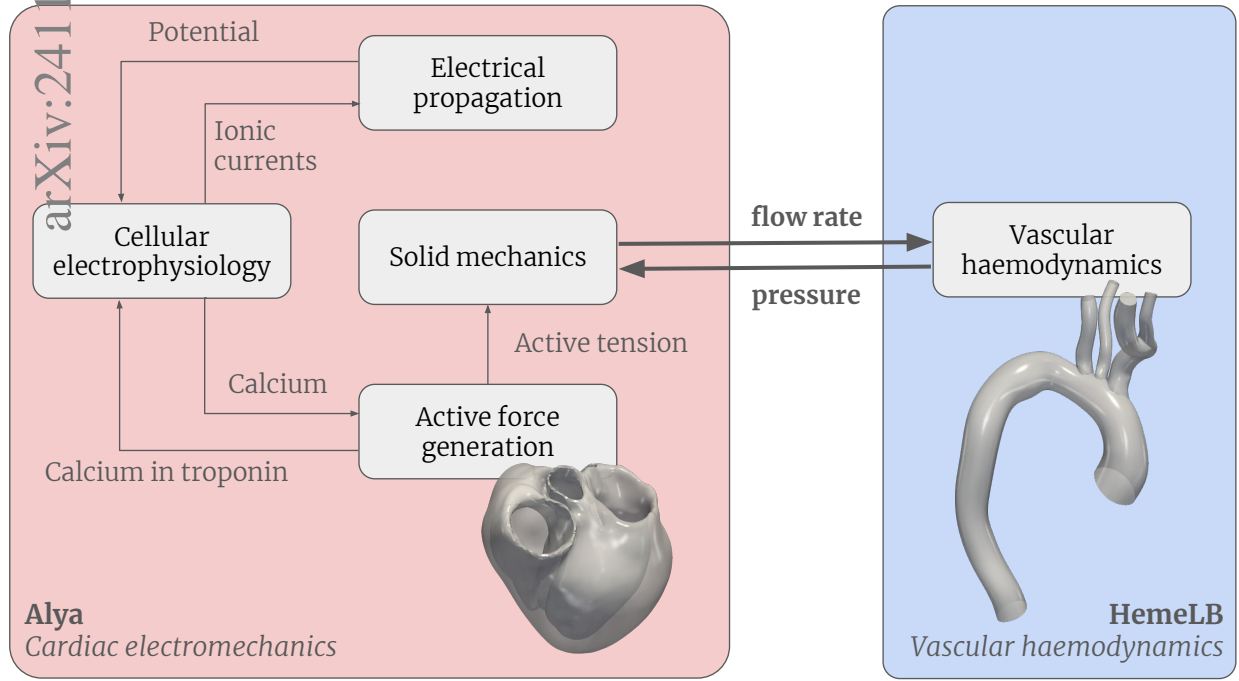


Graphical Abstract

A Multi-Component, Multi-Physics Computational Model for Solving Coupled Cardiac Electromechanics and Vascular Haemodynamics

Sharp C. Y. Lo, Alberto Zingaro, Jon W. S. McCullough, Xiao Xue, Mariano Vázquez, Peter V. Coveney



Highlights

A Multi-Component, Multi-Physics Computational Model for Solving Coupled Cardiac Electromechanics and Vascular Haemodynamics

Sharp C. Y. Lo, Alberto Zingaro, Jon W. S. McCullough, Xiao Xue, Mariano Vázquez, Peter V. Coveney

- Innovative approach couples 3D cardiac and vascular simulations
- Multi-component strategy leverages existing specialised solvers
- Coupled model highlights influence of detailed vascular flow on cardiac function
- File-based partitioned coupling scheme requires minimal extra computation time
- Framework facilitates virtual human models and digital twins development

A Multi-Component, Multi-Physics Computational Model for Solving Coupled Cardiac Electromechanics and Vascular Haemodynamics

Sharp C. Y. Lo^a, Alberto Zingaro^b, Jon W. S. McCullough^a, Xiao Xue^a, Mariano Vázquez^{b,c}, Peter V. Coveney^{a,d,e}

^aCentre for Computational Science, University College London, London, United Kingdom

^bELEM Biotech SL, Pier07 - Via Laietana, 26, 08003, Barcelona, Spain

^cBarcelona Supercomputing Center, Plaça Eusebi Güell, 1-3, 08034, Barcelona, Spain

^dAdvanced Research Computing Centre, University College London, London, United Kingdom

^eInformatics Institute, Faculty of Science, University of Amsterdam, Amsterdam, Netherlands

Abstract

The circulatory system, comprising the heart and blood vessels, is vital for nutrient transport, waste removal, and homeostasis. Traditional computational models often isolate individual biophysical processes, such as cardiac electromechanics and blood flow dynamics, failing to capture the system's integrated nature. This paper presents an innovative approach that couples a 3D electromechanical model of the heart with a 3D fluid mechanics model of vascular blood flow. Our file-based partitioned coupling scheme allows these models to run independently while sharing essential data through intermediate files. We validate this approach using two solvers: one for cardiac electromechanics and the other for vascular blood flow. Developed by separate research groups, these solvers emphasise different dynamical scales and utilise distinct discretisation schemes. Numerical simulations using idealised and realistic anatomies show that the implemented coupling scheme is reliable and requires minimal additional computation time relative to advancing individual time steps in the heart and blood flow models. Notably, the coupled model predicts muscle displacement differently than the standalone heart model, highlighting the influence of detailed vascular blood flow on cardiac function. This study presents a paradigm case of how to build virtual human models and digital twins by productive collaboration between teams with complementary expertise.

Keywords: circulatory system, cardiovascular simulation, partitioned coupling scheme, high-fidelity simulation, high-performance computing, digital twin

1. Introduction

The circulatory system, comprising the heart and blood vessels, is a complex network that operates through a series of tightly coupled biophysical processes occurring at different levels. Key among these processes are electrophysiology, solid mechanics, and fluid dynamics. As an electrical impulse spreads through cardiomyocytes, calcium ions are released from intracellular stores, bind to troponin C, and trigger heart muscle contraction [1, 2]. The increased pressure within the ventricles causes the atrioventricular valves to close and the semilunar valves to open, resulting in the ejection of blood from the ventricles into the arteries [3]. The circulation of blood in the vascular network, facilitated by vessel constriction and dilation, ensures nutrient transport, waste removal, and homeostasis [3]. Understanding these individual processes, as well as their interactions, is crucial for advancing medical research and clinical interventions.

Email address: p.v.coveney@ucl.ac.uk (Peter V. Coveney)

Mathematical and numerical modelling has become an indispensable approach to describing biophysical processes in the cardiovascular system [4, 5, 6, 7, 8, 9]. In the context of the heart, cardiomyocyte models are essential for characterising the flow of ions across cellular and intracellular membranes [10, 2, 1]. The extension of these models to include gap junctions between adjacent cells enables the simulation of ionic currents in the myocardium, providing a comprehensive view of cardiac electrophysiology [10, 2, 1]. Moreover, various mechanical models have been proposed to describe the motion of the heart, elucidating deformation patterns, stress distribution, and the mechanical properties of cardiac tissues [11, 12, 13, 14]. Recent advancements in multi-physics models have integrated electrophysiology and solid mechanics to accurately reflect the excitation-contraction coupling that occurs within the myocardium [15, 16, 17, 18, 19]. Regarding the vasculature, fluid dynamic models are used to simulate blood flow in vessels, providing insights into shear stress distribution, pressure gradients, and flow features [20, 21, 22, 23, 24, 25]. Various mechanical models have also been employed to analyse the behaviour of vessel walls [26, 27, 28, 29]. Moreover, advancements in multi-physics models have coupled fluid dynamics and solid mechanics to capture the interplay between blood flow and wall motion [30, 31, 32, 33, 34]. These models collectively enhance our understanding of cardiovascular physiology.

To fully characterise human cardiac function and blood transport, it is essential to consider the complex interactions between the heart and blood vessels. However, most existing models focus on one organ and make simplifying assumptions about the other. Typically, detailed cardiac function models use reduced-order models to represent blood circulation [15, 35, 36, 18, 37], while detailed vascular blood flow models often prescribe a profile of cardiac outflow, based on measurements, statistics, or theories [38, 39, 40, 25]. Although these assumptions reduce computational costs, neglecting the feedback mechanism between the two subsystems is likely to impair the accuracy of the biophysical processes described. In contrast, a multi-component model, which integrates high-fidelity representations of the biophysical components, offers a more realistic and comprehensive description of the full system.

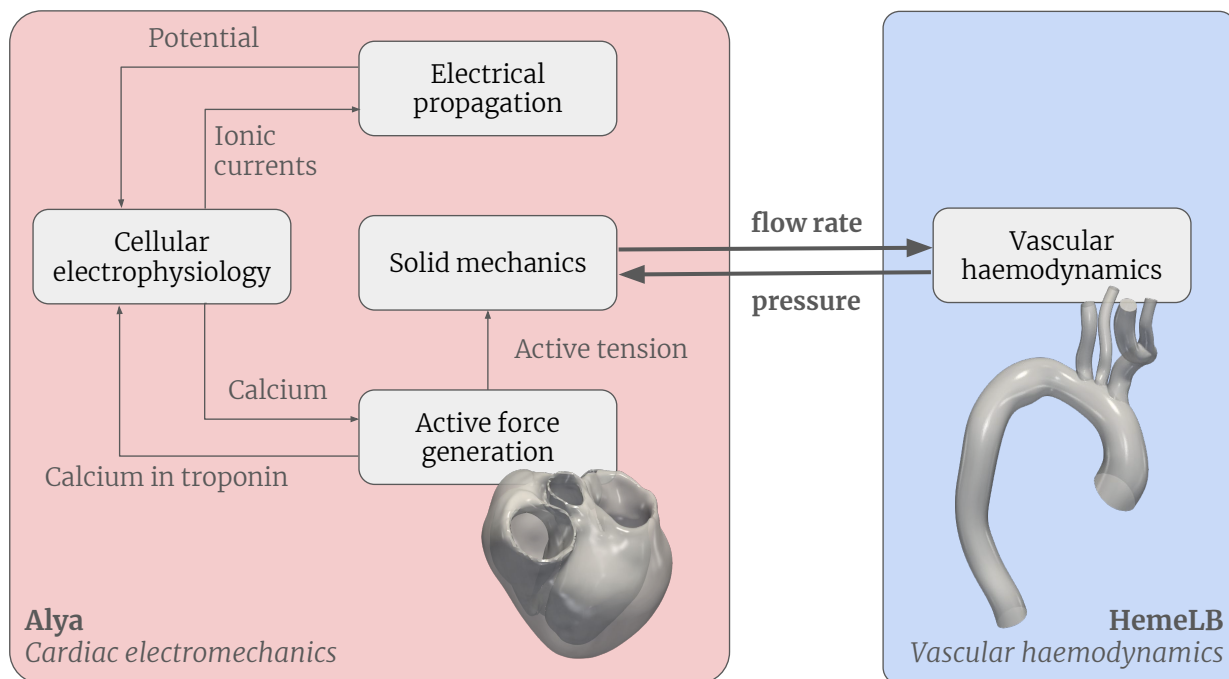


Figure 1: The coupled multi-component, multi-physics human cardiovascular model constructed in this work.

In this paper, we present an innovative approach to couple a 3D electromechanical model

of the heart with a 3D fluid mechanics model of the blood vessels (see Figure 1). We adopt a multi-component coupling strategy rather than rewriting everything into a new, monolithic code, leveraging existing specialised solvers to build a more comprehensive model. To address this complexity, we employ a file-based partitioned coupling scheme, which couples the two models by alternately writing and reading data through intermediate files. This approach allows each model to run independently while sharing essential simulation data, thereby maintaining optimal computational performance.

We establish the validity of this approach by using Alya [41, 5] to model cardiac electromechanics and HemeLB [42, 43] to model vascular blood flow. These models have been developed by separate research groups, emphasise different dynamical scales, and utilise distinct discretisation schemes. By leveraging the excellent scaling performance of these models on supercomputers, this study aims to construct an efficient multi-component, multi-physics model of the cardiovascular system. Moreover, it illustrates how a virtual human [44], also referred to as a human digital twin, can be developed by integrating efforts from different research groups working in complementary, specialised fields.

The subsequent sections of this paper are structured as follows. In Section 2, we present the individual and coupled models of cardiac function and blood flow, along with the simulation tests designed to verify the coupled model. In Section 3, we analyse the results of these tests, focusing on the computational aspects of the coupled model, and discuss the differences between the solutions obtained from the coupled model and those from the individual models. In Section 4, we discuss the limitations of the coupled model. Finally, we conclude our findings in Section 5.

2. Methods

In this section, we first present the electromechanical model of the heart in Section 2.1 and the fluid mechanics model of vascular blood flow in Section 2.2. Then, we describe the coupled model in Section 2.3 and the coupling scheme in Section 2.4. Lastly, we outline the setup of simulation cases for verifying disparate aspects of the coupled model in Section 2.5.

2.1. Electromechanical Model of the Heart in Alya

To model the ventricular electrical activity and mechanical contraction, we use a fully-coupled electromechanical model developed in Alya [41, 5]: a simulation code designed for solving multi-physics problems in engineering applications using finite element method. The code is designed for high-performance computing and has demonstrated scalability up to 100,000 cores [41].

Let $\Omega_0^A \in \mathbb{R}^3$ be the end-diastolic configuration of a left ventricle at time $t = 0$, also representing our *reference configuration*, and T the final time. As we sketch in Figure 2, Ω_0^A is bounded by $\partial\Omega_0^A = \Gamma_{0\text{endo}}^A \cup \Gamma_{0\text{epi}}^A \cup \Gamma_{0\text{base}}^A$, which are the endocardium, epicardium, and base respectively; we denote by \mathbf{n}_0 the outward-pointing normal to the boundary.

We model cardiac electrophysiology via the monodomain equation [45]. Let $v : \Omega_0^A \times (0, T) \rightarrow \mathbb{R}$ be the transmembrane potential, $\mathbf{w} : \Omega_0^A \times (0, T) \rightarrow \mathbb{R}^{n_w}$ the gating variables (with n_w the number of gating variables), and \mathbf{c} the ionic concentrations $\mathbf{c} : \Omega_0^A \times (0, T) \rightarrow \mathbb{R}^{n_c}$ (with n_c the number of ionic concentrations inside of the cell). The monodomain model – coupled to a cellular ionic model – reads:

$$\frac{\partial v}{\partial t} - \nabla \cdot (D \nabla v) + \frac{I_{\text{ion}}(v, \mathbf{w}, \mathbf{c})}{C_m} = \frac{I_{\text{app}}}{C_m} \quad \text{in } \Omega_0^A \times (0, T), \quad (1)$$

$$\frac{d\mathbf{w}}{dt} = \mathbf{W}(v, \mathbf{w}, \mathbf{c}) \quad \text{in } \Omega_0^A \times (0, T), \quad (2)$$

$$\frac{d\mathbf{c}}{dt} = \mathbf{C}(v, \mathbf{w}, \mathbf{c}) \quad \text{in } \Omega_0^A \times (0, T), \quad (3)$$

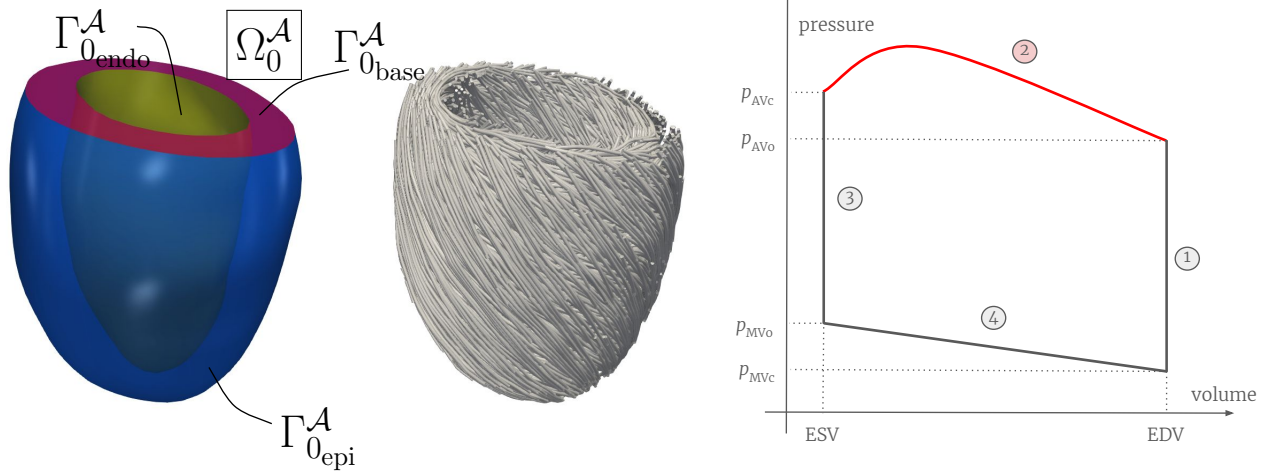


Figure 2: The electromechanical model in Alya. From left to right: left ventricular geometry with its boundary portions, cardiac fibres and pressure-volume loop. In the latter, we highlight in red the ejection phase (phase 2), i.e. where the coupling with HemeLB is carried out.

with homogeneous boundary conditions on the whole boundary. \mathbf{D} is the orthotropic tensor of local diffusivity in the reference configuration expressed, with respect to the tensor of conductivity $\boldsymbol{\sigma}$, as [46]:

$$\mathbf{D} = \frac{\boldsymbol{\sigma}}{C_m S_v} = \frac{1}{C_m S_v} \left(\sigma_f \tilde{\mathbf{f}}_0 \otimes \tilde{\mathbf{f}}_0 + \sigma_s \tilde{\mathbf{s}}_0 \otimes \tilde{\mathbf{s}}_0 + \sigma_n \tilde{\mathbf{n}}_0 \otimes \tilde{\mathbf{n}}_0 \right),$$

where σ_f , σ_s , and σ_n are the conductivity in the fibre, sheet and normal directions and $\tilde{\mathbf{f}}_0$, $\tilde{\mathbf{s}}_0$, and $\tilde{\mathbf{n}}_0$ the unit vector field expressing their directions. Cardiac fibres are modelled with Laplace-Dirichlet rule-based methods [47, 48], as depicted in Figure 2. C_m is the membrane capacitance per unit area and S_v the surface-to-volume ratio. $I_{\text{app}}(\mathbf{X}, t)$ is the applied current; \mathbf{W} and \mathbf{C} are the right-hand sides of the system of ODEs corresponding to \mathbf{w} and \mathbf{c} , respectively. The term I_{ion} collects the ionic currents. For the cellular ionic model, we use the one introduced by O'Hara et al. [49] and incorporate the modifications proposed by Passini et al. [50] and the modified conductance as described by Dutta et al. [51].

Let $\Phi : \Omega_0^{\mathcal{A}} \times (0, T) \rightarrow \mathbb{R}^3$ be a deformation operator which maps each point \mathbf{X} of the reference configuration $\Omega_0^{\mathcal{A}}$ onto the *current configuration* $\Omega_t^{\mathcal{A}} = \Phi(\Omega_0^{\mathcal{A}}, t)$, for all $t \in (0, T)$, so that each point of the current configuration is $\mathbf{x}(\mathbf{X}, t) = \Phi(\mathbf{X}, t)$. We define the displacement field $\mathbf{d} : \Omega_0^{\mathcal{A}} \times (0, T) \rightarrow \mathbb{R}^3$ as $\mathbf{d}(\mathbf{X}, t) = \mathbf{x}(\mathbf{X}, t) - \mathbf{X}$, the deformation tensor $F(\mathbf{X}, t) = \frac{\partial \Phi}{\partial \mathbf{X}}$, and $S(\mathbf{d}, t)$ is the second Piola-Kirchhoff stress tensor. J is the determinant of F : $J = \det(F) > 0$. The mechanical deformation is modelled by Cauchy's first equation of motion equipped with initial and boundary conditions:

$$\rho_0^{\mathcal{A}} \frac{\partial^2 \mathbf{d}}{\partial t^2} - \nabla \cdot (FS(\mathbf{d})) = \mathbf{0} \quad \text{in } \Omega_0^{\mathcal{A}} \times (0, T), \quad (4)$$

$$FS(\mathbf{d})\mathbf{n}_0 = (k_{\text{epi}} \mathbf{d} \cdot \mathbf{n}_0) \mathbf{n}_0 \quad \text{on } \Gamma_{0\text{epi}}^{\mathcal{A}} \times (0, T), \quad (5)$$

$$\mathbf{d} \cdot \hat{\mathbf{e}}_x = \mathbf{d} \cdot \hat{\mathbf{e}}_y = 0 \quad \text{on } \Gamma_{0\text{base}}^{\mathcal{A}} \times (0, T), \quad (6)$$

$$FS(\mathbf{d})\mathbf{n}_0 = -p_{\text{endo}} J F^{-\top} \mathbf{n}_0 \quad \text{on } \Gamma_{0\text{endo}}^{\mathcal{A}} \times (0, T), \quad (7)$$

$$\mathbf{d} = \mathbf{0} \text{ and } FS(\mathbf{d}) = \mathbf{0} \quad \text{in } \Omega_0^{\mathcal{A}} \times \{0\}, \quad (8)$$

where $\rho_0^{\mathcal{A}}$ is the tissue density. We consider an active stress formulation, for which we can decompose S into an active and a passive term. The excitation-contraction coupling is modelled

using the active force generation model introduced by Land et al. [52]. For the passive part, we consider the Holzapfel and Ogden constitutive law [53].

We set a null initial condition in terms of both displacement and stress, as expressed in equation 8. In equation 5, we set Robin-type boundary conditions on the epicardium with k_{epi} the corresponding normal spring stiffness. We orient the ventricular geometry such that the normal to the base coincides with the z axis. On the base, we set the displacement to zero in the x and y direction, leaving a stress-free condition in the remaining direction z . In equation 6, \hat{e}_x and \hat{e}_y are the unit vectors in the x and y directions, respectively. On the endocardium, as expressed in equation 7, we set a Neumann boundary condition with the time-dependent ventricular blood pressure $p_{\text{endo}}(t)$. To model the latter, we subdivide the heartbeat into four phases: isovolumetric contraction, ejection, isovolumetric relaxation, and filling (see Figure 2). After an initialization phase that allows the cardiac muscle to be brought to the time of end-diastole, we model each phase of the heartbeat as follows [54]:

1. *Isovolumetric contraction*: starting from end-diastole configuration, when the ventricular volume stops increasing ($\frac{dV}{dt} \leq 0$), the mitral valve closes, the ventricle contracts and the pressure increases keeping a constant volume equal to the end-diastolic volume (EDV). We integrate in time the following laws:

$$\frac{dp_{\text{endo}}(t)}{dt} = -c_1 \frac{dV(t)}{dt} - c_2 \frac{d^2V(t)}{dt^2},$$

where V is the ventricular volume; c_1 and c_2 are two coefficients that allow us to keep the condition of constant volume. The second term, acting on the second-order volume derivative, stabilizes potential spurious oscillations in the pressure [54].

2. *Ejection* starts when the ventricular pressure overcomes the systemic arterial pressure: $p_{\text{endo}} \geq p_{\text{AVo}}$, where p_{AVo} is prescribed. The aortic valve opens, the muscle keeps contracting and the ventricular volume decreases. This dynamics is modelled using a two-element Windkessel (WK2) model [55, 56]:

$$C^{\mathcal{A}} \frac{dp_{\text{endo}}(t)}{dt} + \frac{1}{R^{\mathcal{A}}} p_{\text{endo}}(t) = - \frac{dV(t)}{dt},$$

where $R^{\mathcal{A}}$ represents the total resistance of the arterial network and $C^{\mathcal{A}}$ the compliance.

3. *Isovolumetric relaxation* starts when the ventricular volume stops decreasing: $\frac{dV(t)}{dt} \geq 0$: the aortic valve closes ($p_{\text{endo}} = p_{\text{AVc}}$), the ventricle relaxes, the pressure decreases at a constant volume equal to the end-systolic volume (ESV). We integrate in time the following law:

$$\frac{dp_{\text{endo}}(t)}{dt} = -r_1 \frac{dV(t)}{dt} - r_2 \frac{d^2V(t)}{dt^2},$$

where r_1 and r_2 are two coefficients that allow us to keep the volume constant.

4. *Filling*: when the ventricular pressure reaches the atrial pressure $p_{\text{endo}} \leq p_{\text{MVo}}$ (where p_{MVo} is prescribed), the mitral valve opens, and the filling phase (from the atrium to the ventricle) starts. The ventricular pressure is modelled with the following decay equation:

$$\frac{dp_{\text{endo}}(t)}{dt} = -\gamma \frac{dV(t)}{dt},$$

where γ is a decay constant.

In our baseline electromechanical simulation (Test 0), i.e. using Alya in a standalone fashion, we model the endocardial pressure as explained above. When we couple Alya with HemeLB, as we shall discuss in Section 2.3, the endocardial pressure is instead given by HemeLB in each time step.

Spatial discretisation is carried out with linear finite elements. We use a first-order Yanenko operator splitting scheme and the implicit Euler time advancing scheme for electrophysiology (see [5] for additional details). We solve the non-linear mechanical problem with the Newton-Raphson scheme. Time discretisation of the mechanical problem is carried out with the Newmark scheme using the Rayleigh-damping method to damp potential spurious oscillations [57, 5].

2.2. Fluid Mechanics Model of Vascular Blood Flow in HemeLB

The 3D blood flow in vessels is simulated using HemeLB [42, 58], an open-source fluid flow solver based on the lattice Boltzmann method (LBM) [59, 60]. This solver was verified and validated in previous works examining vascular flows [61, 62, 63]. HemeLB has been developed into versions optimised for CPU and GPU architectures, Both versions have demonstrated excellent scaling characteristics on high-performance computers: the CPU version has utilised over 300,000 CPU cores, while the GPU version has leveraged over 18,000 GPUs [43]. In this study, we use the CPU version of HemeLB [64].

Established on the basis of kinetic theory, the LBM solves for the velocity distribution function f of fluid particles at the mesoscopic scale in the Boltzmann equation rather than the fluid density ρ , flow velocity \mathbf{U} , and fluid pressure P at the macroscopic scale [59, 60]. Discretisation of the Boltzmann equation over an isotropic lattice gives the lattice Boltzmann equation

$$f_i(t + \Delta t^{\mathcal{H}}, \mathbf{x} + \mathbf{c}_i \Delta t^{\mathcal{H}}) = f_i(t, \mathbf{x}) + \Omega_i(t, \mathbf{x}) \Delta t^{\mathcal{H}}.$$

Here, Ω_i is the collision operator which characterises the interactions occurring between particles, and $\{f_i, i = 0, \dots, q\}$ are the discretised form of f in q different velocities $\{\mathbf{c}_i\}$ [59, 60].

In this work, we use the Bhatnagar-Gross-Krook [65] collision operator $\Omega_i = -(f_i - f_i^{eq})/\tau_0$, which relaxes the distribution functions towards an equilibrium f_i^{eq} with a relaxation time τ_0 , and the D3Q19 velocity set (3D lattice, $q = 19$) [60]. The lattice Boltzmann equation with the Bhatnagar-Gross-Krook collision operator, known as the LBGK equation, reads [65, 60, 59]

$$f_i(t + \Delta t^{\mathcal{H}}, \mathbf{x} + \mathbf{c}_i \Delta t^{\mathcal{H}}) = f_i(t, \mathbf{x}) - \frac{\Delta t^{\mathcal{H}}}{\tau_0} \left[f_i(t, \mathbf{x}) - f_i^{eq}(t, \mathbf{x}) \right]. \quad (9)$$

This equation corresponds to the incompressible Navier-Stokes equations

$$\nabla \cdot \mathbf{U} = 0, \quad (10a)$$

$$\frac{\partial \mathbf{U}}{\partial t} + (\mathbf{U} \cdot \nabla) \mathbf{U} = -\frac{1}{\rho} \nabla P + \nabla \cdot (\nu_0 \nabla \mathbf{U}), \quad (10b)$$

with a dynamic viscosity ν_0 given by

$$\nu_0 = c_s^2 \left(\tau_0 - \frac{\Delta t^{\mathcal{H}}}{2} \right), \quad (11)$$

when the Mach number

$$Ma = \|\mathbf{U}\|/c_s \quad (12)$$

is sufficiently low ($\ll 1$), where $c_s = (1/\sqrt{3})\Delta x^{\mathcal{H}}/\Delta t^{\mathcal{H}}$ is the speed of sound [59, 60]. Using the distribution functions, the macroscopic variables can be calculated as

$$\rho = \sum_{i=0}^q f_i, \quad (13)$$

$$\mathbf{U} = \frac{1}{\rho} \sum_{i=0}^q f_i \mathbf{c}_i, \quad (14)$$

$$P = \rho c_s^2. \quad (15)$$

In general, the Mach number is non-zero and the Navier-Stokes equations reproduced by the LBM are weakly compressible. The compressibility errors associated with the LBGK model typically scale with $\mathcal{O}(Ma^2)$. Because of these errors, the density fluctuates around an average value $\rho_0^{\mathcal{H}}$, which corresponds to the reference pressure P_{ref} of the fluid:

$$P_{\text{ref}} = \rho_0^{\mathcal{H}} c_s^2. \quad (16)$$

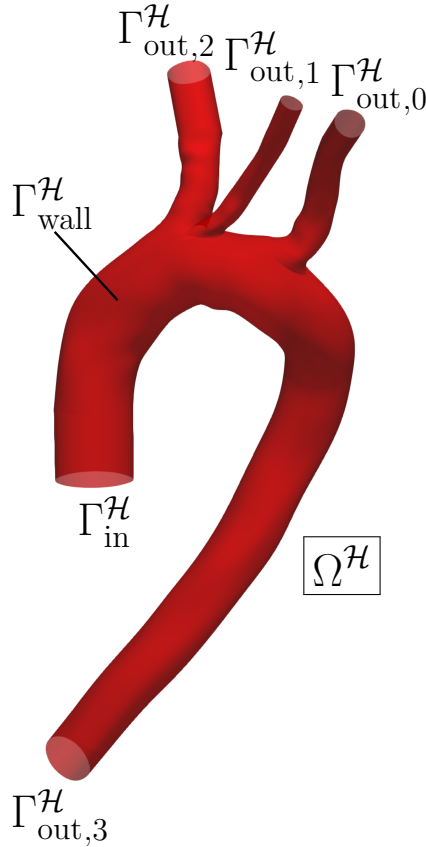


Figure 3: The thoracic aorta model for HemeLB in Test 2. It is adapted from the 0012_H_AO_H model in the Vascular Model Repository [66] produced from a computed tomography angiogram of a 26-year-old male human. The fluid domain $\Omega^{\mathcal{H}}$ is the interior of this model bounded by the vessel wall $\Gamma_{\text{wall}}^{\mathcal{H}}$, an inlet $\Gamma_{\text{in}}^{\mathcal{H}}$, and four outlets $\{\Gamma_{\text{out},i}^{\mathcal{H}}, i = 0, 1, 2, 3\}$.

Let $\Omega^{\mathcal{H}} \in \mathbb{R}^3$ be the fluid domain of a vascular model. It is bounded by the vessel wall $\Gamma_{\text{wall}}^{\mathcal{H}}$, an inlet $\Gamma_{\text{in}}^{\mathcal{H}}$, and a group of outlets $\Gamma_{\text{out}}^{\mathcal{H}} = \{\Gamma_{\text{out},i}^{\mathcal{H}}\}$. As an illustration, the arterial model used in this study is shown in Figure 3.

In the fluid domain, $\Omega^{\mathcal{H}}$, the blood is assumed to be Newtonian with a constant dynamic viscosity (ν_0) of 0.0035 Pa s [67] and a constant density ($\rho_0^{\mathcal{H}}$) of 1050 kg m⁻³ [68]. The vessel walls, $\Gamma_{\text{wall}}^{\mathcal{H}}$, are assumed to be rigid by imposing the Bouzidi-Firdaouss-Lallemand boundary condition [69] on the walls, $\Gamma_{\text{wall}}^{\mathcal{H}}$.

The inlet section, $\Gamma_{\text{in}}^{\mathcal{H}}$, serves as the coupling interface in all simulations conducted in this study. The inlet flow rate Q_{in} , provided by Alya through coupling, is used to calculate the flow velocity at each lattice site on the inlet plane, as described in our previous work [70]. The velocity is assumed to be perpendicular to the inlet plane and follows a parabolic profile:

$$\mathbf{U}(r, t) = \frac{g(r)}{\int_{\Gamma_{\text{in}}^{\mathcal{H}}} g(r) \, dA} Q_{\text{in}}(t) \hat{\mathbf{n}}, \quad (17)$$

where $\hat{\mathbf{n}}$ is the unit normal vector, A denotes the area, and

$$g(r) = 1 - \frac{r^2}{r_{\text{max}}^2} \quad (18)$$

is a function of the distance r between the lattice site and the inlet centre. On the edge of the inlet plane where $r = r_{\text{max}}$, this function equals zero to satisfy the no-slip boundary condition. The speed is then imposed as an inlet condition using Ladd's approach [71].

At the outlet sections, $\Gamma_{\text{out}}^{\mathcal{H}}$, the Nash pressure boundary condition is imposed [61]. The pressure P is calculated from the flow rate Q using the WK2 model [55, 56], where the flow rate is obtained by integrating the flow velocity in the normal direction over the outlet plane. Using a semi-explicit scheme to discretise the WK2 model equation [72], the pressure at time step $n + 1$ is given by

$$P^{[n+1]} = \frac{R^{\mathcal{H}} C^{\mathcal{H}}}{R^{\mathcal{H}} C^{\mathcal{H}} + \Delta t^{\mathcal{H}}} P^{[n]} + \frac{R^{\mathcal{H}} \Delta t^{\mathcal{H}}}{R^{\mathcal{H}} C^{\mathcal{H}} + \Delta t^{\mathcal{H}}} Q^{[n]}, \quad (19)$$

where $R^{\mathcal{H}}$ and $C^{\mathcal{H}}$ represent the resistance and capacitance of peripheral vessels respectively. The choice of these parameters is different in the simulations for different tests and is therefore provided individually in Sections 2.5.2 and 2.5.3.

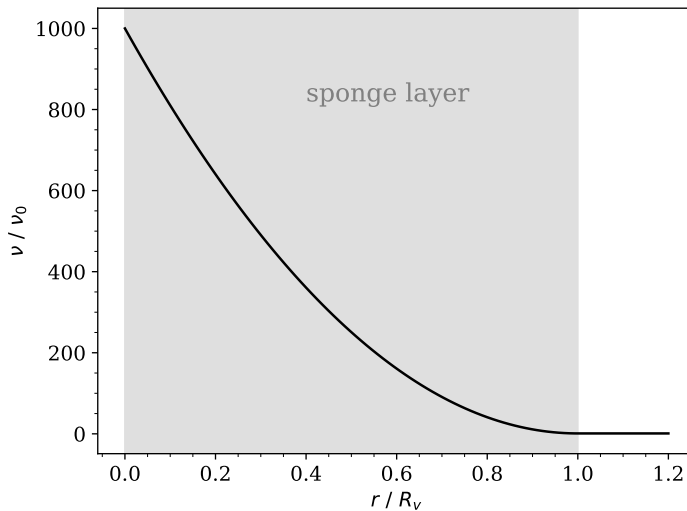


Figure 4: Viscosity ν within a viscous sponge layer as a function of the distance from the outlet centre r , normalised by the base dynamic viscosity ν_0 and the radius of the sponge layer R_v respectively. The amplification factor of the viscosity ν/ν_0 smoothly increases from 1 on the sponge layer surface ($r = R_v$) to 1000 at the outlet centre ($r = 0$).

We include viscous sponge layers around the outlets to prevent reflections from the boundaries [73]. Each outlet is surrounded by a spherical sponge layer with a radius R_v at its midpoint. Within the sponge layer ($r \leq R_v$), the dynamic viscosity ν gradually increases from the base

value ν_0 at the spherical surface ($r = R_v$) to the maximum value ν_{\max} at the centre ($r = 0$). This variation is described by a function of the distance from the outlet centre r as

$$\nu(r) = \nu_0 + (\nu_{\max} - \nu_0) \left(\frac{r}{R_v} - 1 \right)^2 \quad (20)$$

and plotted in Figure 4. In this study, the ratio ν_{\max}/ν_0 is set to 1000, as in other studies [73, 74, 75]. The change in viscosity is implemented by adjusting the relaxation time, according to their relationship given in equation 11, as follows:

$$\tau(r) = \frac{1}{2} + \frac{\nu(r)}{c_s^2}. \quad (21)$$

Outside the sponge layer ($r > R_v$), both the viscosity and the relaxation time remain at their base values ν_0 and τ_0 respectively.

In an incompressible flow, the gradient rather than the value of the fluid pressure is what matters, as evidenced in equation 10b; however, in this coupled system involving mechanics, the pressure value itself becomes important due to its physical role. To ascertain this value within the fluid flow, the reference pressure, P_{ref} , is set in HemeLB. This reference is chosen to be close to the pressure on the endocardium before the coupling starts to prevent large oscillations in the solutions.

2.3. Coupled Model

We couple the two models during the ejection phase only (corresponding to phase 2 mentioned in Section 2.1). Thus, for the coupling, we restrict the time domain to $[t_0, t_f]$, where t_0 and t_f are the initial and final time instants of the ejection phase. Before the coupling begins, one heartbeat is simulated as a warm-up. Similarly, the flow velocity is increased steadily from zero to the value just before the coupling phase starts.

To express the whole coupled model at a continuum level, we first compactly denote the ventricular electromechanical model — solved in Alya — as

$$\mathcal{A}(v, \mathbf{w}, \mathbf{c}, \mathbf{d}; p_{\text{endo}}) = 0 \quad \text{in } \Omega_0^{\mathcal{A}} \times [t_0, t_f], \quad (22a)$$

consisting of the gathering of equations 1–3 and 4–8. Similarly, we compactly denote the vascular hemodynamics model — solved in HemeLB — as

$$\mathcal{H}(\mathbf{U}, P; Q_{\text{in}}) = 0 \quad \text{in } \Omega^{\mathcal{H}} \times [t_0, t_f], \quad (22b)$$

composed of equations 9, 14 and 15.

The two models are coupled by enforcing the dynamic balance and kinematic continuity. For the continuity of stresses, we enforce that the endocardial ventricular pressure p_{endo} on $\Gamma_{0_{\text{endo}}}^{\mathcal{A}}$ equals the average pressure at the inlet section $\Gamma_{\text{in}}^{\mathcal{H}}$. This dynamic balance is formulated as

$$p_{\text{endo}}(t) = \frac{1}{\Gamma_{\text{in}}^{\mathcal{H}}} \int_{\Gamma_{\text{in}}^{\mathcal{H}}} P(\mathbf{x}, t) \, d\mathbf{x} \quad \text{in } \Gamma_{0_{\text{endo}}}^{\mathcal{A}} \times [t_0, t_f]. \quad (22c)$$

Analogously, velocity continuity is enforced by assuming that the decreased rate of ventricular volume V_{LV} equals the inlet flow rate Q_{in} across $\Gamma_{\text{in}}^{\mathcal{H}}$. This kinematic continuity is formulated as

$$Q_{\text{in}}(t) = -\frac{dV_{\text{LV}}(\mathbf{d})}{dt} \quad \text{in } \Gamma_{\text{in}}^{\mathcal{H}} \times [t_0, t_f]. \quad (22d)$$

Altogether, equations 22a – 22d represent the fully coupled model at the continuum level.

A low-pass filter is implemented on the coupling interface to attenuate the spurious oscillations in the flow when needed. The flow rate value Q_{in} given by Alya is passed through a

simple RC circuit and results in the flow rate value \tilde{Q}_{in} imposed at the inlet of the HemeLB domain. The relation between these flow rate values is governed by

$$Q_{\text{in}}(t) - \tilde{Q}_{\text{in}}(t) = RC \frac{d\tilde{Q}_{\text{in}}(t)}{dt}, \quad (23)$$

where R and C are the resistance and capacitance of the RC circuit. The flow rate imposed at the inlet, \tilde{Q}_{in} , remains constant until Q_{in} is updated by Alya. By discretising this equation in time and rearranging the terms, we obtain

$$\tilde{Q}_{\text{in}}^{[n+1]} = \alpha Q_{\text{in}}^{[n+1]} + (1 - \alpha) \tilde{Q}_{\text{in}}^{[n]}, \quad (24)$$

where $\alpha = \Delta t^A / (RC + \Delta t^A)$ is a smoothing factor lying within the range $[0, 1]$.

2.4. Partitioned Coupling Scheme between the Two Models

Alya and HemeLB are coupled via a partitioned scheme, wherein their respective model equations are solved independently using exchanged data. During intervals between data exchanges, Alya and HemeLB independently solve their model equations 22a and 22b using the exchanged data p_{endo} and Q_{in} as the boundary values on the coupling interfaces, respectively. In addition, Alya computes the flow rate Q_{in} on $\Gamma_{0_{\text{endo}}}^A$ and transmits it to HemeLB, while HemeLB determines the pressure p_{endo} on Γ_{in}^H and shares it with Alya.

The data exchange is achieved by file writing and reading mechanisms. Specifically, two intermediate files, File A and File B, are created in the working directory. File A is used to exchange p_{endo} , while File B is used for Q_{in} . This approach requires minimal changes in both codes, allowing for swift implementation.

Since Alya and HemeLB focus on different dynamic scales, the time step sizes required for the simulations differ. Therefore, allowing the coupling to occur at various frequencies in the two solvers is important. This capability is implemented in our algorithm by controlling the parameter k , defined as the ratio of the time step size of Alya to that of HemeLB, i.e. $k = \Delta t^A / \Delta t^H$. This ratio is greater than or equal to one because the electromechanics model in Alya operates on a larger dynamic scale than the mesoscopic fluid dynamics scale in HemeLB. In addition, this ratio is defined as an integer so that the boundary value in Alya is updated at every time step. Let $m \in [0, k - 1]$ be an iteration index. Each time HemeLB completes a time step, m is incremented by one. When m reaches k , HemeLB updates the value of Q_{in} from File B and resets m to zero. This ensures that data exchange occurs once per time step of Alya and once every k time steps of HemeLB. The algorithm for this coupling scheme is outlined in Algorithm 1.

2.5. Simulation Tests

We conduct three simulation tests to study different aspects of the proposed coupled model. Test 0 sets the baseline solution of the heart electromechanics for subsequent comparisons with the coupled model. Test 1 verifies the coupling scheme using simplified geometries. Test 2 demonstrates the feasibility of the coupled model within physiological contexts.

2.5.1. Test 0: Left Ventricle

In this test, we perform a standalone simulation using Alya. We use the results of this simulation to (i) determine the reference pressure P_{ref} of the fluid domain of HemeLB and (ii) compare the results with those obtained from the coupled Alya-HemeLB simulations. The geometry for this simulation represents the left ventricle, which is based on a 3D model of the human heart produced from computed tomography and magnetic resonance imaging scans and created by Zygote [76]. The endocardial pressure during the ejection phase is determined by the WK2 model, as detailed in Section 2.1. The time step size Δt^A is set to 10^{-4} s for both electrophysiology and mechanics. The parameters of the physics models used in Alya are given in Table 1.

Algorithm 1 Algorithm for coupling Alya with HemeLB during the ejection phase.

```

1: Initialise  $p_{\text{endo}}^{[0]}$  and  $Q_{\text{in}}^{[0]}$  at time step  $n = 0$ .
2: while  $n < (t_f - t_0)/\Delta t^A$  do
3:   Alya reads  $p_{\text{endo}}^{[n]}$  from File A.
4:   Alya solves heart electromechanics (eq. 22a) at time step  $n$  using  $p_{\text{endo}}^{[n]}$  for the endocar-
      dial boundary condition (eq. 7).
5:   Alya calculates  $Q_{\text{in}}^{[n]}$  using eq. 22d.
6:   Alya writes  $Q_{\text{in}}^{[n]}$  to File B
7:   Alya waits for  $p_{\text{endo}}^{[n+1]}$  to be available in File A.
8:   HemeLB reads  $Q_{\text{in}}^{[n]}$  from File B.
9:   Calculate  $\tilde{Q}_{\text{in}}^{[n]}$  using eq. 24.
10:  Initialise  $m \leftarrow 0$ .
11:  while  $m < k$  do
12:    HemeLB solves vascular haemodynamics (eq. 22b) at time step  $n + (m + 1)/k$  using
       $\tilde{Q}_{\text{in}}^{[n]}$  for the inlet boundary condition (eq. 17).
13:    HemeLB calculates  $p_{\text{endo}}^{[n+(m+1)/k]}$  using eq. 22c.
14:     $m \leftarrow m + 1$ .
15:  end while
16:  HemeLB writes  $p_{\text{endo}}^{[n+1]}$  to File A.
17:  HemeLB waits for  $Q_{\text{in}}^{[n+1]}$  to be available in File B.
18:   $n \leftarrow n + 1$ .
19: end while

```

2.5.2. Test 1: Left Ventricle with Cylinder

In the first test, we verify the coupling scheme, focusing on its implementation and computational aspects. Specifically, we check whether the coupling occurs at the correct time steps and whether the values exchanged at the coupling interface are consistent in Alya and HemeLB. The simulation domains include the same left ventricle geometry as in Test 0 and a cylinder representing the aorta.

A physiological cardiac output poses tight constraints on the parameters of the fluid flow simulation. First, for a given flow rate, the flow speed is inversely proportional to the area of the inlet. Second, according to equation 12, the Mach number is proportional to the flow speed, the time step size, and the inverse of the voxel size. However, the LBGK model requires that the non-dimensionalised relaxation time, $\tau_0/\Delta t^{\mathcal{H}}$, is not close to 0.5 for numerical stability [60]. According to equation 11, the dynamic viscosity is proportional to the square of the voxel size and the inverse of the time step size. These relations result in the competing conditions that

- (i) increasing the voxel size will decrease the Mach number and the relaxation time;
- (ii) increasing the time step size will increase the Mach number and the relaxation time; and
- (iii) increasing the inlet area will increase the Mach number but decrease the relaxation time.

The above constraints lead to the following choice of parameters. A cylinder of radius 0.02 m and a height of 0.2 m is used, as shown in Figure 5. It is voxelised to a resolution ($\Delta x^{\mathcal{H}}$) of $1.67 \cdot 10^{-4}$ m so that there are about 120 lattice sites along a radius. The time step size $\Delta t^{\mathcal{H}}$ is varied between $2.5 \cdot 10^{-5}$ s and $1.0 \cdot 10^{-5}$ s to check the implementation of the coupling scheme. These values correspond to a coupling frequency of $k = \{4, 5, 8, 10\}$ given the time step size of 10^{-4} s for Alya. In particular, we study the solutions obtained from the simulation

Table 1: Parameters and their corresponding descriptions, unit measures, and values for different physics models used in Alya to carry out the electromechanical simulations. For additional details on the parameters used in the electromechanical model, we refer readers to ref. [54].

Physics	Parameter	Description	Unit	Value
Electrophysiology	D	Diffusivity in the fibers, normal and sheet directions	cm^2/ms	0.03, 0.01, 0.01
	I_{app}	Applied current	$\mu\text{A}/\text{cm}^2$	-40
	C_m	Membrane capacitance per unit area	$\mu\text{F}/\text{cm}^2$	1
Haemodynamics	c_1	First coefficient for isovolumetric contraction	barye/ml	0.05
	c_2	Second coefficient for isovolumetric contraction	barye s / ml	10
	C^A	Compliance of Windkessel model for ejection	ml/barye	0.001
	R^A	Resistance of Windkessel model for ejection	barye s / ml	1500
	r_1	First coefficient for isovolumetric relaxation	barye/ml	0.1
	r_2	Second coefficient for isovolumetric relaxation	barye s / ml	1
	γ	Decay constant for ventricular filling	barye / ml	-500
	p_{AVo}	opening pressure of aortic valve	barye	11998.8
	p_{MVo}	opening pressure of mitral valve	barye	8000

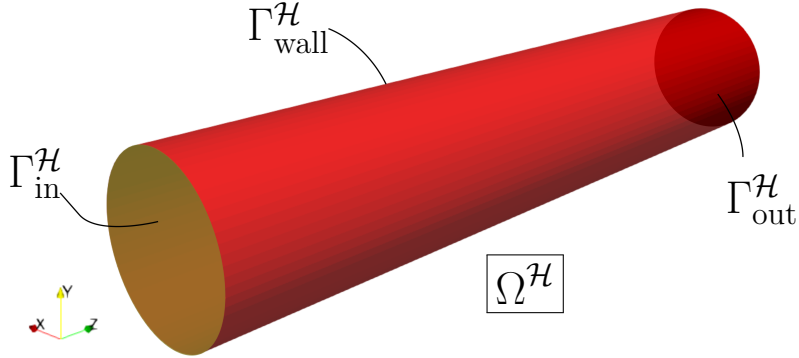


Figure 5: The cylinder model for HemeLB in Test 1. The fluid domain $\Omega^{\mathcal{H}}$ is the interior of this model bounded by the wall $\Gamma_{\text{wall}}^{\mathcal{H}}$, an inlet $\Gamma_{\text{in}}^{\mathcal{H}}$, and an outlet $\Gamma_{\text{out}}^{\mathcal{H}}$.

with $\Delta t^{\mathcal{H}} = 2.5 \cdot 10^{-5}$ s, or $\tau_0/\Delta t^{\mathcal{H}} = 0.5108$. For a physiological cardiac output resulting in a maximum flow rate of around $0.5 \text{ dm}^3/\text{s}$, the maximum velocity assuming a quadratic profile is 0.796 m/s . The corresponding Mach number of 0.208 is considered to contribute to a small compressibility error [60].

In addition, the resistance and capacitance parameters of the WK2 model at the outlet are set to $1.5 \cdot 10^8 \text{ Pa s/m}^3$ and $10^6 \text{ m}^3/\text{Pa}$, respectively. The viscous sponge layer enclosing the outlet is set to have a radius of $R_v = 0.04 \text{ m}$, which is two times that of the cylinder.

To check that the data exchanged, p_{endo} and Q_{in} , are consistent in Alya and HemeLB, we

compare their values at the coupling interface. In particular, we compare the output values of these variables in post-processing instead of the values exchanged during the coupling to ensure that the values are not only transmitted correctly but also implemented correctly as the boundary conditions in the models.

2.5.3. Test 2: Left Ventricle with Thoracic Aorta

In the second test, we evaluate the coupled model in a physiologically sound setting. We use the same left ventricle model for Alya as in the first test but employ a thoracic aorta model for HemeLB. This arterial model, shown in Figure 3, is adapted from the 0012_H_AO_H model in the Vascular Model Repository [66], which was produced from a computed tomography angiogram of a 26-year-old male human. The model includes the ascending aorta, the descending aorta, and three branches: brachiocephalic, left common carotid, and left subclavian arteries. The original model is scaled up by 1.25 times in all dimensions to ensure the inlet radius approximates the normal size for adults (0.015 m [77, 78]). In addition, the inlet and outlets are elongated by one to two times their diameters to mitigate instabilities caused by the boundary conditions [79].

Table 2: Parameters of the two-element Windkessel model imposed at the outlets of the thoracic aorta model.

	Outlet 0	Outlet 1	Outlet 2	Outlet 3
Resistance ($\text{kg m}^{-4} \text{s}^{-1}$)	$3.422 \cdot 10^9$	$4.182 \cdot 10^9$	$1.176 \cdot 10^9$	$2.543 \cdot 10^8$
Capacitance ($\text{m}^4 \text{s}^2 \text{kg}^{-1}$)	$3.443 \cdot 10^{-10}$	$2.817 \cdot 10^{-10}$	$1.002 \cdot 10^{-9}$	$4.632 \cdot 10^{-9}$

The fluid domain for HemeLB is created by voxelising [80] the thoracic aorta model to obtain a three-dimensional uniform grid of lattice sites. A voxel size of $\Delta x^{\mathcal{H}} = 10^{-4}$ m is used, resulting in about 150 lattice sites along a radius of the inlet. The time step size $\Delta t^{\mathcal{H}}$ is set to $6.25 \cdot 10^{-6}$ s, or $\tau_0/\Delta t^{\mathcal{H}} = 0.50625$, which corresponds to a coupling frequency of $k = 16$ given the time step size of 10^{-4} s for Alya. For a physiological cardiac output resulting in a maximum flow rate of around $0.5 \text{ dm}^3/\text{s}$, the maximum velocity assuming a quadratic profile is 1.42 m/s . The corresponding Mach number of 0.153 is considered to contribute to a small compressibility error [60].

The low-pass filter with an appropriate smoothing factor α as described in equation 24 is applied to stabilise the simulation. The parameters of the WK2 model at the outlets are obtained using the method we introduced previously [70, 81] and the flow rate ratios $5.5 : 4.5 : 16 : 74$ for Outlets 0 to 3, respectively [82]. The resulting parameters, listed in Table 2, have the same order of magnitude as those found in similar studies of the aorta [83, 84]. The radius of the viscous sponge layer, R_v , is set to 0.03 m at all outlets so that it encloses two times the largest outlet, which has an equivalent radius of 0.0115 m .

3. Results and Discussion

In this section, we present and analyse the results of the three simulation tests in Sections 3.1 – 3.3. Lastly, we assess the computational efficiency of the coupled model. All our simulations are performed on the ARCHER2 UK national supercomputer (<https://www.archer2.ac.uk>).

3.1. Test 0: Left Ventricle

We perform the standalone simulation of Alya for two heartbeats. We present the results in the second heartbeat since the electromechanical model usually requires some beats to reach a periodic solution. The simulation results are shown in Figure 6, presenting the time series of cardiac pressure and volume as well as the displacement of heart muscles at the end of the ejection phase. Additionally, the endocardial pressure immediately before the ejection phase in

the second heartbeat suggests a reference pressure P_{ref} of 68 mmHg for the fluid domain in the subsequent tests.

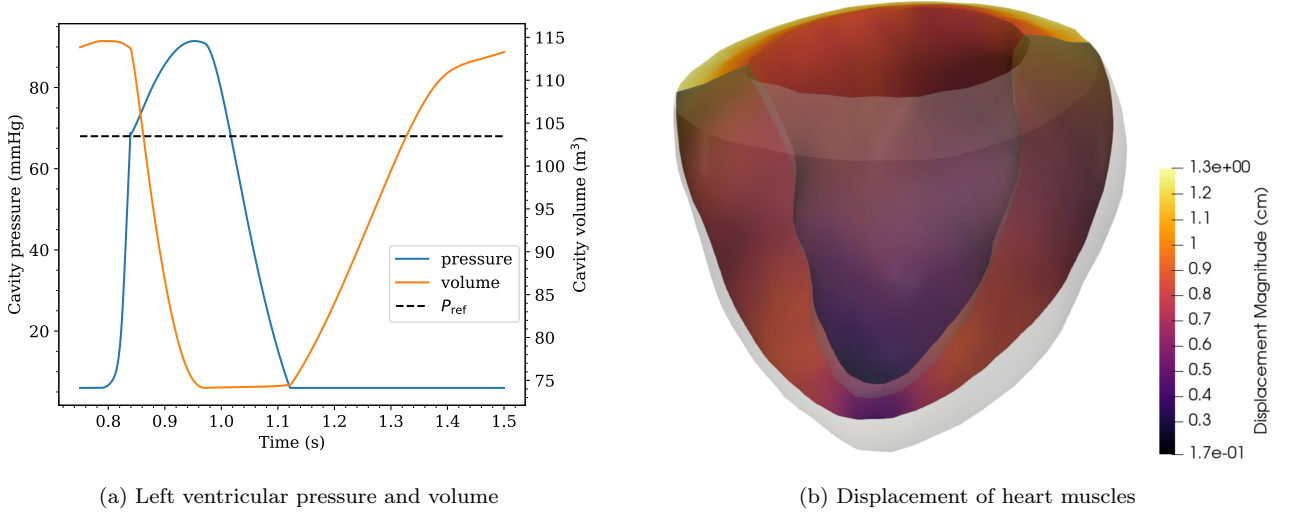


Figure 6: (a) Left ventricular pressure and volume and (b) displacement of heart muscles at the end of the ejection phase ($t = 0.97$ s) in the standalone simulation of Alya. The left ventricular pressure immediately before the ejection phase suggests a reference pressure P_{ref} of 68 mmHg for the fluid domain in the subsequent tests.

3.2. Test 1: Left Ventricle with Cylinder

Here we present the results of the coupled simulations using the left ventricle and cylinder geometries. First of all, we assess the reliability of the coupling scheme. To test the implementation of the coupling, we perform the coupled simulations using different time step sizes and coupling frequencies in HemeLB while keeping them fixed in Alya. These simulations are completed at the specified simulation times, showing that our implementation of the coupling algorithm is reliable.

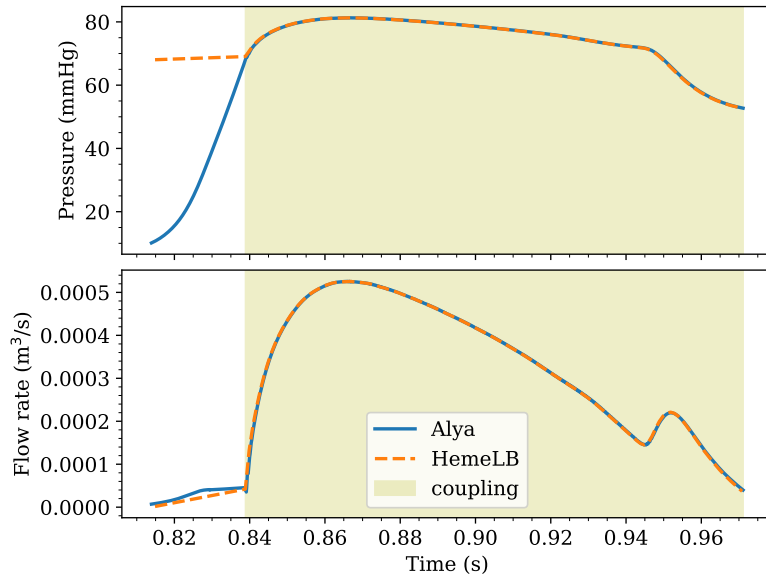


Figure 7: Pressure and flow rate values used by Alya and HemeLB at the coupling interface. The results show that the values are consistent in the two codes during coupling.

Second, we check the consistency of the exchanged data. In the following, we focus on the simulation with $k = 4$. The pressure and flow rate values output by Alya and HemeLB at the coupling interface are shown in Figure 7. During the coupling phase, the outputs agree very well for pressure and flow rate. This suggests the data exchanged are consistent in the two solvers and that our implementation of the coupling algorithm is correct.

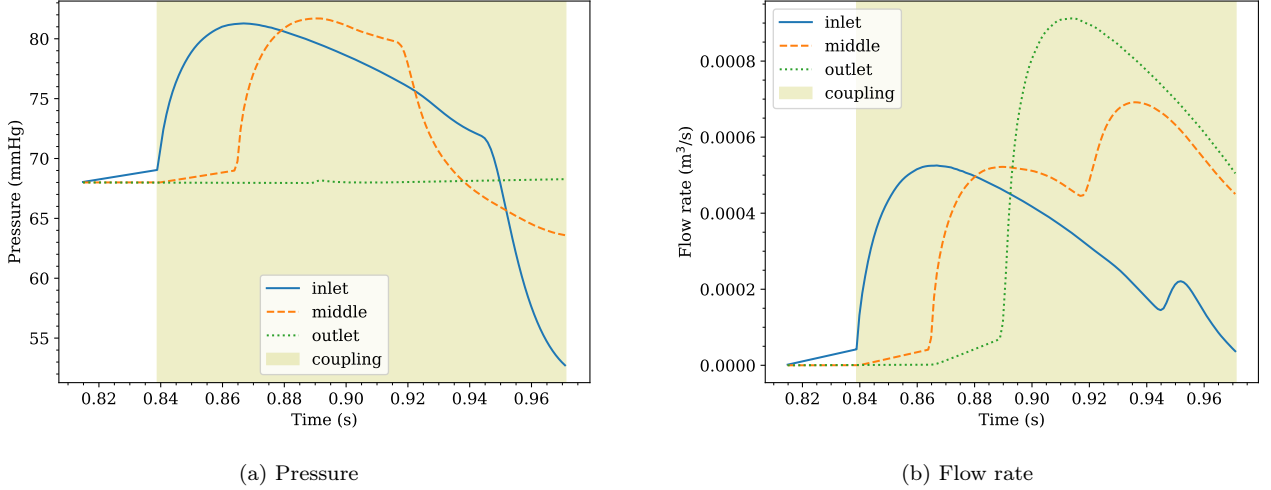


Figure 8: (a) Pressure and (b) flow rate on the inlet, middle, and outlet planes of the cylinder domain. The variables are influenced by wave reflection and the viscous sponge layer around the outlet.

Third, we evaluate the stability of the coupled simulation. The pressure and flow rate at the inlet, middle, and outlet of the fluid domain are plotted in Figure 8. As shown in the figure, these flow variables remain bounded throughout the simulation. The same is observed for the solutions of Alya. We found that the WK2 model and the viscous sponge layer at the fluid outlet effectively dampen numerical oscillations in the flow, thereby stabilising the simulation.

3.3. Test 2: Left Ventricle with Thoracic Aorta

Here we present the results of the simulations using the left ventricle and thoracic aorta geometries. Initially, the coupled simulations become unstable at the tested coupling frequencies ($k = 8, 10, 12, 14, 16, 20$). However, applying the low-pass filter with an appropriate smoothing factor (α), all these simulations become stable. This demonstrates the effectiveness of the low-pass filter in stabilising the coupled model for this specific system. In the following, we look into the simulation using $k = 16$ and $\alpha = 0.05$. The maximum Mach number in this simulation is 0.246, remaining below the recommended limit to ensure acceptable compressibility errors [60].

We examine the flow on different cross-sections of the aorta, namely the inlet and planes A to D (see Figure 10 for their locations). The plots in Figure 9 show that the pressure generally decreases as the flow moves downstream, while the flow rate attains a similar peak. The successive peaks for the inlet, planes A, B, C, and D, indicate the capture of wave propagation in the blood, which is observed in physiological humans [85]. Wave propagation is simulated because the LBM solves for a weakly compressible flow, allowing for slight changes in fluid density (see equation 13).

To gain more insights into the flow dynamics, we visualise the flow velocity on planes A to D. Figure 10 displays the magnitude of the normal velocity and the directions of the tangential velocity on these planes at the ejection peak ($t = 0.88$ s). For all planes, the flow directions largely follow the shape of the vessels. For planes A and C, the flow accelerates as it flows over the bend, as suggested by the higher normal speed on the inner side. For plane B, the flow splits, with one direction leading upward towards the neck and the other downward into the

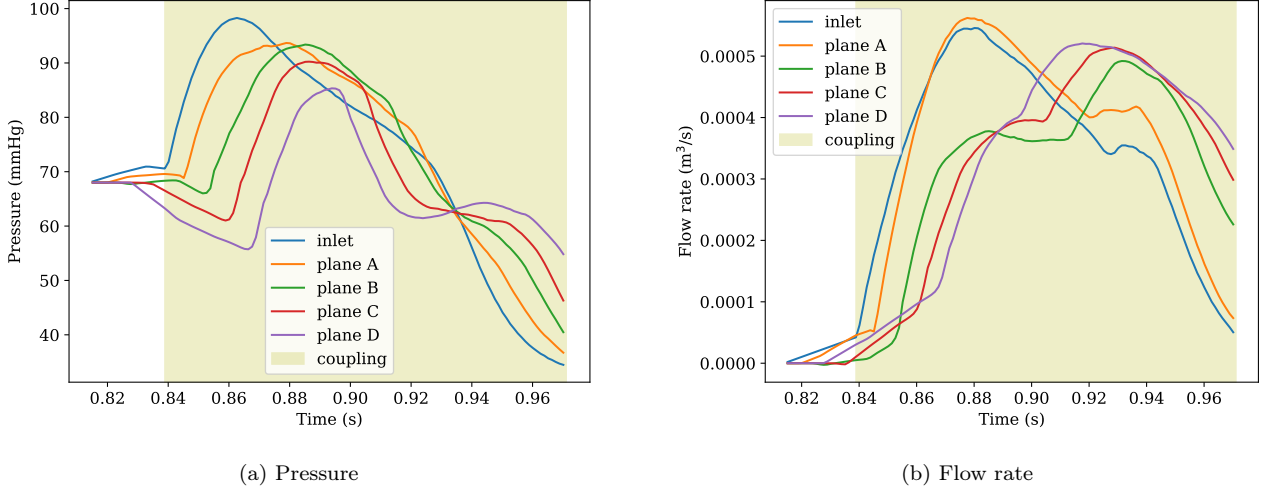


Figure 9: (a) Pressure and (b) flow rate on the inlet and planes A to D of the aorta domain. The results are obtained from the simulation using $k = 4, \alpha = 1.0$.

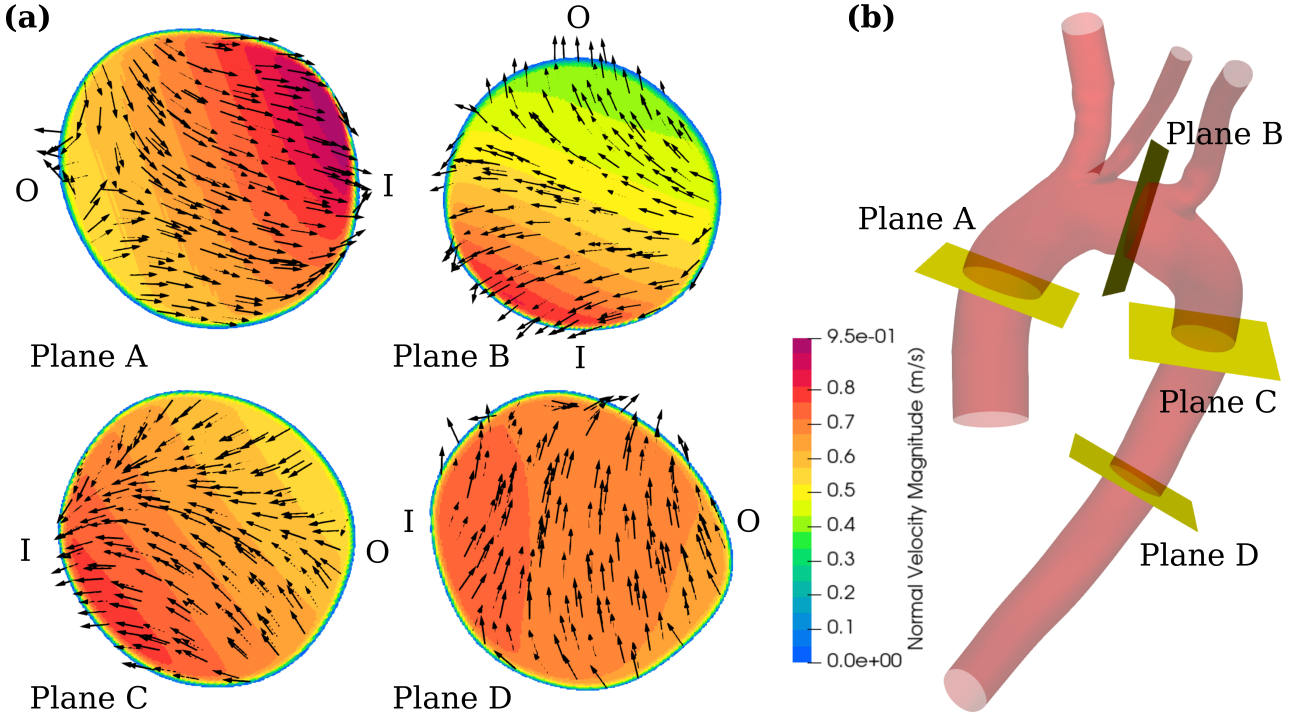


Figure 10: (a) Flow velocity at the ejection peak ($t = 0.88$ s) on (b) different cross-sections of the aorta. The heat map illustrates the magnitude of the normal velocity, while the arrows indicate the directions of the tangential velocity. The labels "O" and "I" indicate the outer and inner sides of the aorta, respectively.

descending aorta. These results are comparable to those observed at peak systole in studies examining aortic blood flow [84, 83].

In addition, we visualise the displacement of heart muscles and blood pressure within the aorta during the ejection peak. As shown in Figure 11, the muscle contraction is more pronounced at the ventricle base and decreases towards the tip. Simultaneously, a high-pressure front originates from the inlet and propagates downstream. Around the outlets, the effects of the sponge layer are observed, where the pressure is lower than the surroundings. The coupled model effectively captures the 3D structures of muscle contraction and blood flow within the vessels as well as their dynamic interactions.

Furthermore, we compare the displacement of heart muscles at the end of the ejection phase with the baseline solution in Test 0. The results from these tests (Figures 6b and 12a) indicate

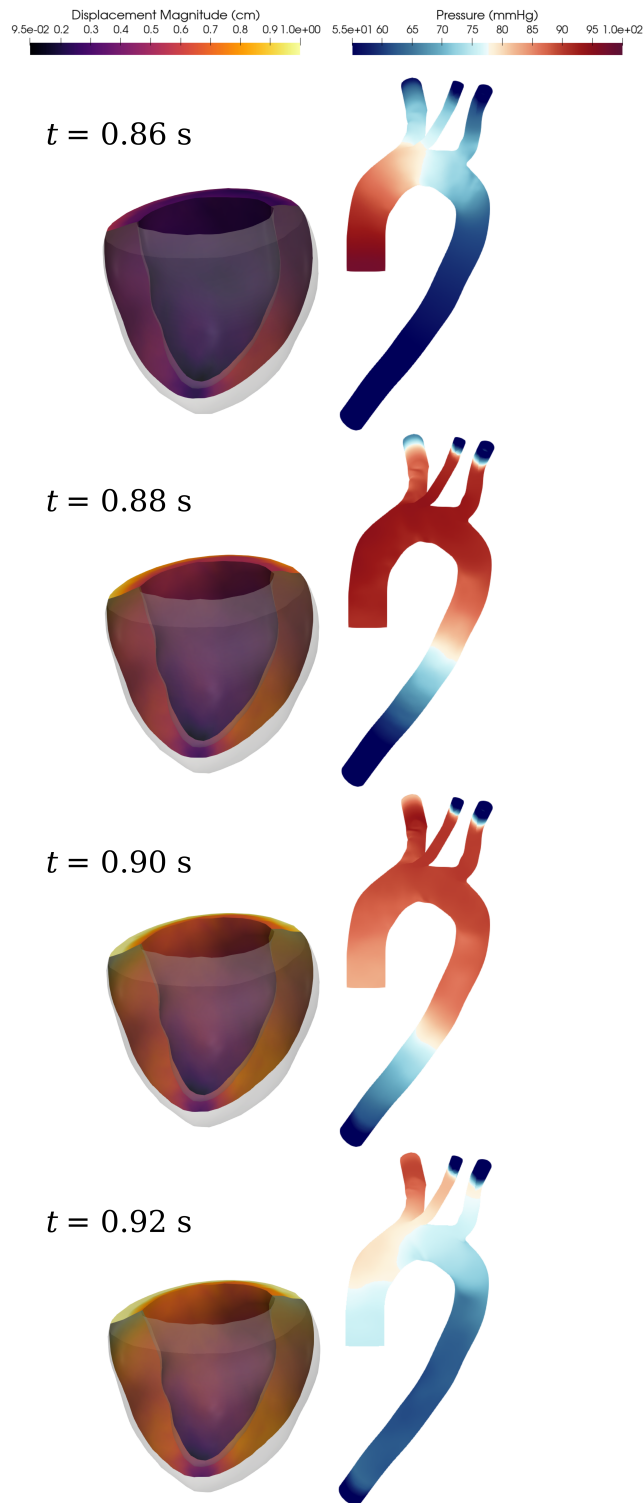


Figure 11: Displacement of heart muscles and blood pressure within the aorta during the ejection peak. The coupled model effectively captures the 3D structures of muscle contraction and vascular blood flow as well as their dynamical interactions.

a similar distribution of muscle displacement. However, the displacement in Test 2 ranges from 0.17 cm to 1.27 cm, whereas in Test 0 it ranges from 0.25 cm to 1.30 cm. As shown in Figure 12b, the differences between the two solutions generally decrease from the base to the tip and from the epicardium to the endocardium, with the greatest differences observed in the middle of the endocardium. These differences underscore the importance of accurately prescribing pressure values on the endocardium, which is determined by vascular blood flow.

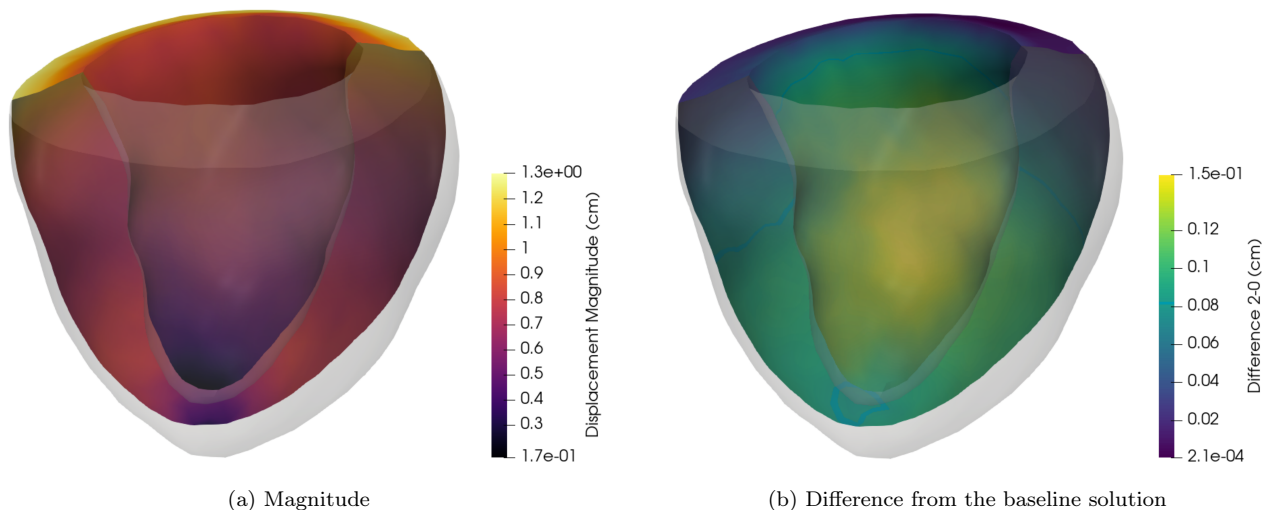


Figure 12: (a) The magnitude of displacement of heart muscles at the end of the ejection phase ($t = 0.97$ s) and (b) the difference compared with the baseline solution, i.e. solution from Test 2 minus that from Test 0).

Since Alya and HemeLB are coupled in a staggered manner, the scalability of the coupled model is entirely determined by the scalability of the individual solvers, which has been extensively demonstrated in previous studies [41, 43]. The coupling scheme, which performs data exchange by reading and writing two small files (each containing only two numbers), runs sequentially. As a result, the time spent on coupling remains relatively constant and minimal. When Alya runs on two compute nodes and HemeLB on 64 nodes, the percentage of the time spent on coupling relative to the elapsed time per time step is about 4 % for Alya and 6 % for HemeLB (see Appendix A for more details).

4. Limitations

A primary limitation of the coupled model presented in this study is the inherent necessity of assuming a specific spatial velocity distribution for inflow into the vasculature (see equation 17). This assumption is required because the flow rate provided by Alya only specifies the total normal velocity at the inlet, leaving the local direction and magnitude of the velocity unspecified. Although the parabolic-shaped profile used in this study (equation 18) may have limited effects on the flow downstream in a healthy aorta due to the accumulated influence of vessel walls, it can significantly impact the flow near the inlet of a diseased aorta, where velocity patterns are highly complex [84, 83]. Ultimately, the spatial velocity profile at the aortic root should be determined by the blood flow dynamics within the heart. Achieving this goal will require incorporating a fluid dynamics model for the heart compartments, coupling the movement of the endocardium with blood flow, and mapping the flow variables between the heart compartments and vascular models. This comprehensive model can be developed through the integration of existing models using multi-component coupling.

Another limitation is the application of a low-pass filter for the flow rate (equation 24) to stabilise the coupled simulations. This numerical technique is necessitated by two main factors. The first is the competing conditions discussed in Section 2.3, which stem from the limitations of the LBGK model when used to simulate flows with a high Reynolds number [60]. The second factor is the stability requirements of the coupling scheme. While a partitioned coupling scheme reduces computational complexity and cost by dividing the system into smaller subsystems and making certain assumptions, it potentially compromises the stability of the coupling [86, 87, 30]. Future studies could improve the stability by using an implicit coupling

scheme and sub-iterating two biophysical models within a time step until the solutions converge. This approach may avoid the need for numerical stabilisation methods and reduce the number of assumptions required in the present work.

A third limitation is that the cardiac electromechanics and vascular haemodynamics are coupled only during the ejection phase. This is the phase during which the aortic valve is open and the flow velocity at the inlet is primarily unidirectional. In other cardiac phases, the closure of the aortic valve means that the vascular flow is governed by the residual impulse, resulting in secondary flow patterns that necessitate a more detailed analysis of the inlet velocity distribution [88, 89, 83, 38]. However, a complete description of heart function and blood transport requires coupling throughout the entire cardiac cycle.

5. Conclusion

We have successfully constructed a 3D model of the cardiovascular system by coupling the 3D electromechanical model of the heart in Alya with the 3D fluid mechanics model of vascular blood flow in HemeLB. Our file-based partitioned coupling scheme has been tested using idealised and realistic anatomies, demonstrating reliability and effectiveness. The implementation of a viscous sponge layer for blood flow and a low-pass filter at the coupling interface has proven effective in stabilising the coupled simulations. Notably, our coupled model predicts muscle displacement differently than the standalone heart model, highlighting the critical role of detailed vascular blood flow modelling in cardiac simulations. The coupling scheme is also efficient, requiring minimal additional computation time relative to advancing individual time steps in the heart and blood flow models.

Looking ahead, this coupled model can be further tested by applying it to a wide range of pathophysiological conditions, such as heart failure, hypertension, and congenital heart defects. Future work can also explore the integration of additional physiological systems, such as the respiratory and nervous systems, to enhance the fidelity of virtual human models and digital twins. Moreover, advancements in computational power and algorithms will likely allow for real-time simulations, thereby broadening the practical applications of these models in clinical decision-making and personalised medicine.

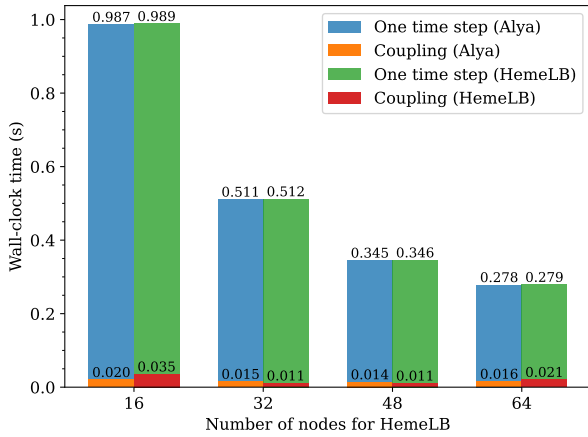
This study exemplifies the successful multi-component coupling of models developed by separate research groups, underscoring the collaborative nature of scientific research. By bridging different modelling approaches, we have laid the groundwork for the development of virtual human models and digital twins which encompasses various biophysical processes within the human body. This integrative effort paves the way for more sophisticated and comprehensive simulations of human physiology, which will ultimately be essential in both research and clinical settings [90].

Appendix A. Computational Performance of the Coupling Scheme

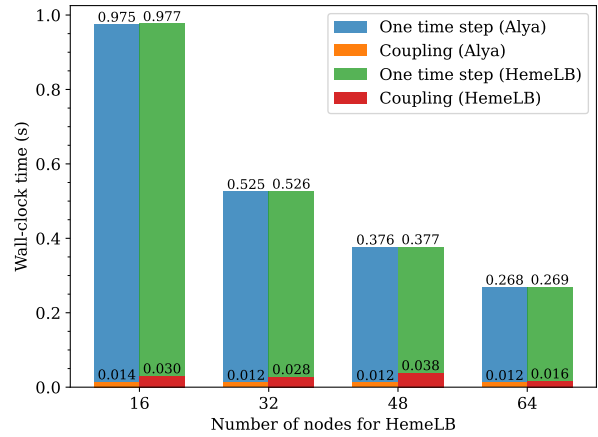
We evaluate the computational performance of the coupling scheme by comparing the time spent on coupling with the time taken for one time step in each solver during the coupling phase.

We record the elapsed time of each time step in Alya and HemeLB and calculate their averages in the coupling phase. To determine the time spent on coupling, we measure the total time required to perform all procedures related to coupling, including the time for writing and reading data in files and the latency, and calculate its average. We perform these measurements using the problem outlined in Test 2.

To understand the effects of parallelisation on the efficiency of the coupling scheme, we vary the number of CPU cores (or compute nodes) used by Alya and HemeLB. The results of the measurements are presented in Figure A.13. While the average elapsed time for one time



(a) One compute node for Alya



(b) Two compute nodes for Alya

Figure A.13: Average wall-clock time per time step and coupling time in Alya and HemeLB using various numbers of compute nodes. The results are shown for Alya using (a) one compute node and (b) two compute nodes with each compute node consisting of 128 CPU cores.

step decreases with the number of compute nodes used for HemeLB, the average time spent on coupling in Alya and HemeLB remains relatively constant between 0.01 s and 0.04 s. For the largest number of nodes tested, specifically two nodes for Alya and 64 nodes for HemeLB, the percentage of the time spent on coupling relative to the elapsed time per time step is about 4 % for Alya and 6 % for HemeLB.

CRedit Authorship Contribution Statement

Sharp C. Y. Lo: Conceptualisation, Methodology, Software, Validation, Formal analysis, Investigation, Data curation, Writing — original draft, Visualisation. **Alberto Zingaro:** Conceptualisation, Methodology, Software, Validation, Formal analysis, Investigation, Writing — original draft, review & editing, Visualisation, Supervision. **Jon W. S. McCullough:** Conceptualisation, Methodology, Software, Funding acquisition. **Xiao Xue:** Software, Funding acquisition. **Mariano Vázquez:** Conceptualisation, Writing — review & editing, Supervision, Project administration, Funding acquisition. **Peter V. Coveney:** Conceptualisation, Writing — review & editing, Supervision, Project administration, Funding acquisition.

Declaration of Competing Interest

The authors declare that they have no known competing financial interests or personal relationships that could have appeared to influence the work reported in this paper.

Declaration of Generative AI and AI-assisted Technologies in Scientific Writing

During the preparation of this work the authors used ChatGPT to improve the readability and language of the manuscript. After using this tool, the authors reviewed and edited the content as needed and take full responsibility for the content of the published article.

Data Availability

Supplementary materials including the vascular anatomies and the complete simulation and analysis data are available from the Figshare repository: <https://figshare.com/s/6a820c417ff707510000>.

Acknowledgements

We acknowledge funding support from the European Commission CompBioMed Centre of Excellence (Grant No. 675451 and 823712) and the UK Engineering and Physical Sciences Research Council (EPSRC) under the projects “UK Consortium on Mesoscale Engineering Sciences (UKCOMES)” (Grant No. EP/R029598/1), “Software Environment for Actionable & VVUQ-evaluated Exascale Applications (SEAVEA)” (Grant No. EP/W007711/1), and “CompBioMedX: Computational Biomedicine at the Exascale” (Grant No. EP/X019446/1). S. C. Y. L. is grateful for the research studentship funded by University College London and CBK Sci Con Ltd. A. Z. and M. V. acknowledge the European Union — EIC Project No 190134524: “ELEM Virtual Heart Populations for Supercomputers” (ELVIS). Views and opinions expressed are, however, those of the authors only and do not necessarily reflect those of the European Union or EISMEA. Neither the European Union nor the granting authority can be held responsible for them. This work used the ARCHER2 UK National Supercomputing Service (<https://www.archer2.ac.uk>), made accessible via the EPSRC CompBioMedX project, and resources of the Oak Ridge Leadership Computing Facility, which is a DOE Office of Science User Facility supported under Contract DE-AC05-00OR22725.

References

- [1] N. A. Trayanova, A. Lyon, J. Shade, J. Heijman, Computational Modeling of Cardiac Electrophysiology and Arrhythmogenesis: Toward Clinical Translation, *Physiological Reviews* 104 (2024) 1265–1333. doi:[10.1152/physrev.00017.2023](https://doi.org/10.1152/physrev.00017.2023).
- [2] M. Regnier, M. Childers (Eds.), Familial Cardiomyopathies, volume 2735 of *Methods in Molecular Biology*, Springer US, New York, NY, 2024. URL: <https://link.springer.com/10.1007/978-1-0716-3527-8>. doi:[10.1007/978-1-0716-3527-8](https://doi.org/10.1007/978-1-0716-3527-8).
- [3] G. Pocock, C. D. Richards, D. A. Richards, Human physiology, fifth edit ed., Oxford University Press, Oxford, United Kingdom, 2018.
- [4] A. Quarteroni, L. Dede, A. Manzoni, C. Vergara, Mathematical modelling of the human cardiovascular system, Cambridge Monographs on Applied and Computational Mathematics, Cambridge University Press (2019). doi:[10.1017/9781108616096](https://doi.org/10.1017/9781108616096).
- [5] A. Santiago, J. Aguado-Sierra, M. Zavala-Aké, R. Doste-Beltran, S. Gómez, R. Arís, J. C. Cajas, E. Casoni, M. Vázquez, Fully coupled fluid-electro-mechanical model of the human heart for supercomputers, *International Journal for Numerical Methods in Biomedical Engineering* 34 (2018) 1–30. doi:[10.1002/cnm.3140](https://doi.org/10.1002/cnm.3140).
- [6] S. A. Niederer, J. Lumens, N. A. Trayanova, Computational models in cardiology, *Nature reviews cardiology* 16 (2019) 100–111. doi:[10.1038/s41569-018-0104-y](https://doi.org/10.1038/s41569-018-0104-y).
- [7] M. Bucelli, A. Zingaro, P. C. Africa, I. Fumagalli, L. Dede, A. Quarteroni, A mathematical model that integrates cardiac electrophysiology, mechanics, and fluid dynamics: Application to the human left heart, *International journal for numerical methods in biomedical engineering* 39 (2023) e3678. doi:<https://doi.org/10.1002/cnm.3678>.
- [8] A. Zingaro, M. Bucelli, R. Piersanti, F. Regazzoni, L. Dede, A. Quarteroni, An electromechanics-driven fluid dynamics model for the simulation of the whole human heart, *Journal of Computational Physics* 504 (2024) 112885. doi:<https://doi.org/10.1016/j.jcp.2024.112885>.

- [9] A. Caiazzo, L. Heltai, I. E. Vignon-Clementel, Mathematical modeling of blood flow in the cardiovascular system, in: Quantification of biophysical parameters in medical imaging, Springer, 2012, pp. 39–61. doi:https://doi.org/10.1007/978-3-031-61846-8_3.
- [10] J. Mayourian, E. A. Sobie, K. D. Costa, An introduction to computational modeling of cardiac electrophysiology and arrhythmogenicity, *Methods in Molecular Biology* 1816 (2018) 17–35. doi:[10.1007/978-1-4939-8597-5{_}2](https://doi.org/10.1007/978-1-4939-8597-5{_}2).
- [11] P. J. Hunter, A. D. McCulloch, H. Ter Keurs, Modelling the mechanical properties of cardiac muscle, *Progress in biophysics and molecular biology* 69 (1998) 289–331. doi:[10.1016/S0079-6107\(98\)00013-3](https://doi.org/10.1016/S0079-6107(98)00013-3).
- [12] M. P. Nash, P. J. Hunter, Computational Mechanics of the Heart, *Journal of elasticity and the physical science of solids* 61 (2000) 113–141. URL: <https://doi.org/10.1023/A:1011084330767>. doi:[10.1023/A:1011084330767](https://doi.org/10.1023/A:1011084330767).
- [13] F. Regazzoni, L. Dedè, A. Quarteroni, Active contraction of cardiac cells: a reduced model for sarcomere dynamics with cooperative interactions, *Biomechanics and Modeling in Mechanobiology* 17 (2018) 1663–1686. URL: <https://doi.org/10.1007/s10237-018-1049-0>. doi:[10.1007/s10237-018-1049-0](https://doi.org/10.1007/s10237-018-1049-0).
- [14] T. G. Mythri, S. J. Hossain, J. L. Greenstein, R. L. Winslow, B. Bhattacharya, First-Principles Electrophysiological Models of Cardiac Ventricular Myocytes as a Basis of Multiscale Mechanics of the Heart, *Journal of Engineering Mechanics* 150 (2024) 1–18. doi:[10.1061/jenmdt.emeng-7487](https://doi.org/10.1061/jenmdt.emeng-7487).
- [15] F. Regazzoni, M. Salvador, P. C. Africa, M. Fedele, L. Dedè, A. Quarteroni, A cardiac electromechanical model coupled with a lumped-parameter model for closed-loop blood circulation, *Journal of Computational Physics* 457 (2022) 111083. URL: <https://doi.org/10.1016/j.jcp.2022.111083>. doi:[10.1016/j.jcp.2022.111083](https://doi.org/10.1016/j.jcp.2022.111083).
- [16] C. M. Augustin, A. Neic, M. Liebmann, A. J. Prassl, S. A. Niederer, G. Haase, G. Plank, Anatomically accurate high resolution modeling of human whole heart electromechanics: A strongly scalable algebraic multigrid solver method for nonlinear deformation, *Journal of Computational Physics* 305 (2016) 622–646. URL: <https://www.sciencedirect.com/science/article/pii/S0021999115007226>. doi:<https://doi.org/10.1016/j.jcp.2015.10.045>.
- [17] P. Lafortune, R. Arís, M. Vázquez, G. Houzeaux, Coupled electromechanical model of the heart: Parallel finite element formulation, *International Journal for Numerical Methods in Biomedical Engineering* 28 (2012) 72–86. URL: <https://doi.org/10.1002/cnm.1494>. doi:<https://doi.org/10.1002/cnm.1494>.
- [18] N. A. Trayanova, J. Constantino, V. Gurev, Electromechanical models of the ventricles, *American Journal of Physiology - Heart and Circulatory Physiology* 301 (2011) 279–286. doi:[10.1152/ajpheart.00324.2011](https://doi.org/10.1152/ajpheart.00324.2011).
- [19] M. Strocchi, M. A. F. Gsell, C. M. Augustin, O. Razeghi, C. H. Roney, A. J. Prassl, E. J. Vigmond, J. M. Behar, J. S. Gould, C. A. Rinaldi, M. J. Bishop, G. Plank, S. A. Niederer, Simulating ventricular systolic motion in a four-chamber heart model with spatially varying robin boundary conditions to model the effect of the pericardium, *Journal of Biomechanics* 101 (2020) 109645. URL: <https://www.sciencedirect.com/science/article/pii/S002192902030052X>. doi:<https://doi.org/10.1016/j.jbiomech.2020.109645>.

- [20] N. Xiao, J. D. Humphrey, C. A. Figueroa, Multi-scale computational model of three-dimensional hemodynamics within a deformable full-body arterial network, *Journal of Computational Physics* 244 (2013) 22–40. URL: <http://dx.doi.org/10.1016/j.jcp.2012.09.016>. doi:10.1016/j.jcp.2012.09.016.
- [21] G. Zavodszky, C. Spieker, B. Czaja, B. van Rooij, Cellular Blood Flow Modeling with HemoCell, in: A. Heifetz (Ed.), *High Performance Computing for Drug Discovery and Biomedicine*, Springer US, New York, NY, 2024, pp. 351–368. URL: https://doi.org/10.1007/978-1-0716-3449-3_16. doi:10.1007/978-1-0716-3449-3{_}16.
- [22] N. Wang, I. Benemerito, S. P. Sourbron, A. Marzo, An In Silico Modelling Approach to Predict Hemodynamic Outcomes in Diabetic and Hypertensive Kidney Disease, *Annals of Biomedical Engineering* 52 (2024) 3098–3112. URL: <https://doi.org/10.1007/s10439-024-03573-2>. doi:10.1007/s10439-024-03573-2.
- [23] J. W. S. McCullough, P. V. Coveney, High resolution simulation of basilar artery infarct and flow within the circle of Willis, *Scientific Reports* 13 (2023) 1–11. URL: <https://doi.org/10.1038/s41598-023-48776-0>. doi:10.1038/s41598-023-48776-0.
- [24] M. U. Qureshi, G. D. Vaughan, C. Sainsbury, M. Johnson, C. S. Peskin, M. S. Olufsen, N. A. Hill, Numerical simulation of blood flow and pressure drop in the pulmonary arterial and venous circulation, *Biomechanics and Modeling in Mechanobiology* 13 (2014) 1137–1154. URL: <https://doi.org/10.1007/s10237-014-0563-y>. doi:10.1007/s10237-014-0563-y.
- [25] H. Kamada, M. Nakamura, H. Ota, S. Higuchi, K. Takase, Blood flow analysis with computational fluid dynamics and 4D-flow MRI for vascular diseases, *Journal of Cardiology* 80 (2022) 386–396. doi:10.1016/j.jjcc.2022.05.007.
- [26] A. Coccarelli, J. M. Carson, A. Aggarwal, S. Pant, A framework for incorporating 3D hyperelastic vascular wall models in 1D blood flow simulations, *Biomechanics and Modeling in Mechanobiology* 20 (2021) 1231–1249. URL: <https://doi.org/10.1007/s10237-021-01437-5>. doi:10.1007/s10237-021-01437-5.
- [27] L. Wang, A. Maehara, R. Lv, X. Guo, J. Zheng, K. L. Billiar, G. S. Mintz, D. Tang, Image-Based Finite Element Modeling Approach for Characterizing In Vivo Mechanical Properties of Human Arteries, 2022. doi:10.3390/jfb13030147.
- [28] G. D. Maso Talou, P. J. Blanco, G. D. Ares, C. G. Bezerra, P. A. Lemos, R. A. Feijóo, Mechanical characterization of the vessel wall by data assimilation of intravascular ultrasound studies, *Frontiers in Physiology* 9 (2018) 1–25. doi:10.3389/fphys.2018.00292.
- [29] P. Kalita, R. Schaefer, Mechanical models of artery walls, *Archives of Computational Methods in Engineering* 15 (2008) 1–36. doi:10.1007/s11831-007-9015-5.
- [30] Y. Bazilevs, J. R. Gohean, T. J. Hughes, R. D. Moser, Y. Zhang, Patient-specific isogeometric fluid-structure interaction analysis of thoracic aortic blood flow due to implantation of the Jarvik 2000 left ventricular assist device, *Computer Methods in Applied Mechanics and Engineering* 198 (2009) 3534–3550. URL: <http://dx.doi.org/10.1016/j.cma.2009.04.015>. doi:10.1016/j.cma.2009.04.015.
- [31] V. Filonova, C. J. Arthurs, I. E. Vignon-Clementel, C. A. Figueroa, Verification of the coupled-momentum method with Womersley’s Deformable Wall analytical solution, *International Journal for Numerical Methods in Biomedical Engineering* 36 (2020) 1–23. doi:10.1002/cnm.3266.

- [32] T. Fringand, I. Cheylan, M. Lenoir, L. Mace, J. Favier, A stable and explicit fluid–structure interaction solver based on lattice-Boltzmann and immersed boundary methods, *Computer Methods in Applied Mechanics and Engineering* 421 (2024) 116777. URL: <https://www.sciencedirect.com/science/article/pii/S0045782524000331>. doi:<https://doi.org/10.1016/j.cma.2024.116777>.
- [33] L. A. Mansilla Alvarez, C. A. Bulant, G. D. Ares, R. A. Feijóo, P. J. Blanco, A mid-fidelity numerical method for blood flow in deformable vessels, *Computer Methods in Applied Mechanics and Engineering* 392 (2022) 114654. URL: <https://doi.org/10.1016/j.cma.2022.114654>. doi:[10.1016/j.cma.2022.114654](https://doi.org/10.1016/j.cma.2022.114654).
- [34] F. Syed, S. Khan, M. Toma, Modeling Dynamics of the Cardiovascular System Using Fluid-Structure Interaction Methods, *Biology* 12 (2023). doi:[10.3390/biology12071026](https://doi.org/10.3390/biology12071026).
- [35] C. M. Augustin, M. A. Gsell, E. Karabelas, E. Willemen, F. W. Prinzen, J. Lumens, E. J. Vigmond, G. Plank, A computationally efficient physiologically comprehensive 3D–0D closed-loop model of the heart and circulation, *Computer Methods in Applied Mechanics and Engineering* 386 (2021) 114092. URL: <https://doi.org/10.1016/j.cma.2021.114092>. doi:[10.1016/j.cma.2021.114092](https://doi.org/10.1016/j.cma.2021.114092).
- [36] T. Gerach, S. Schuler, J. Fröhlich, L. Lindner, E. Kovacheva, R. Moss, E. M. Wülfers, G. Seemann, C. Wieners, A. Loewe, Electro-mechanical whole-heart digital twins: A fully coupled multi-physics approach, *Mathematics* 9 (2021). doi:[10.3390/math9111247](https://doi.org/10.3390/math9111247).
- [37] M. Fedele, R. Piersanti, F. Regazzoni, M. Salvador, P. C. Africa, M. Bucelli, A. Zingaro, A. Quarteroni, et al., A comprehensive and biophysically detailed computational model of the whole human heart electromechanics, *Computer Methods in Applied Mechanics and Engineering* 410 (2023) 115983. doi:<https://doi.org/10.1016/j.cma.2023.115983>.
- [38] C. Stokes, D. Ahmed, N. Lind, F. Haupt, D. Becker, J. Hamilton, V. Muthurangu, H. Von Tengg-Kobligk, G. Papadakis, S. Balabani, V. Díaz-Zuccarini, Aneurysmal growth in type-B aortic dissection: assessing the impact of patient-specific inlet conditions on key haemodynamic indices, *Journal of the Royal Society Interface* 20 (2023). doi:[10.1098/rsif.2023.0281](https://doi.org/10.1098/rsif.2023.0281).
- [39] F. Tajeddini, D. A. Romero, Y. X. Huang, T. E. David, M. Ouzounian, C. H. Amon, J. C. Y. Chung, Type B aortic dissection in Marfan patients after the David procedure: Insights from patient-specific simulation, *JTCVS Open* (2024). URL: <https://www.sciencedirect.com/science/article/pii/S2666273624001207>. doi:<https://doi.org/10.1016/j.xjon.2024.04.017>.
- [40] A. Marzo, P. Singh, I. Larrabide, A. Radaelli, S. Coley, M. Gwilliam, I. D. Wilkinson, P. Lawford, P. Reymond, U. Patel, A. Frangi, D. R. Hose, Computational Hemodynamics in Cerebral Aneurysms: The Effects of Modeled Versus Measured Boundary Conditions, *Annals of Biomedical Engineering* 39 (2011) 884–896. URL: <https://doi.org/10.1007/s10439-010-0187-z>. doi:[10.1007/s10439-010-0187-z](https://doi.org/10.1007/s10439-010-0187-z).
- [41] M. Vázquez, G. Houzeaux, S. Koric, A. Artigues, J. Aguado-Sierra, R. Arís, D. Mira, H. Calmet, F. Cucchietti, H. Owen, A. Taha, E. D. Burness, J. M. Cela, M. Valero, Alya: Multiphysics engineering simulation toward exascale, *Journal of Computational Science* 14 (2016) 15–27. URL: <http://dx.doi.org/10.1016/j.jocs.2015.12.007>. doi:[10.1016/j.jocs.2015.12.007](https://doi.org/10.1016/j.jocs.2015.12.007).

- [42] M. D. Mazzeo, P. V. Coveney, HemeLB: A high performance parallel lattice-Boltzmann code for large scale fluid flow in complex geometries, *Computer Physics Communications* 178 (2008) 894–914. doi:[10.1016/j.cpc.2008.02.013](https://doi.org/10.1016/j.cpc.2008.02.013).
- [43] I. Zacharoudiou, J. W. S. McCullough, P. V. Coveney, Development and performance of a HemeLB GPU code for human-scale blood flow simulation, *Computer Physics Communications* 282 (2023) 108548. URL: <https://doi.org/10.1016/j.cpc.2022.108548>. doi:[10.1016/j.cpc.2022.108548](https://doi.org/10.1016/j.cpc.2022.108548).
- [44] A. G. Hoekstra, E. van Bavel, M. Siebes, F. Gijzen, L. Geris, Virtual physiological human 2016: translating the virtual physiological human to the clinic, *Interface Focus* 8 (2018) 20170067. URL: <https://doi.org/10.1098/rsfs.2017.0067>. doi:[10.1098/rsfs.2017.0067](https://doi.org/10.1098/rsfs.2017.0067).
- [45] P. C. Franzone, L. F. Pavarino, S. Scacchi, *Mathematical cardiac electrophysiology*, volume 13, Springer, 2014.
- [46] A. Bueno-Orovio, E. M. Cherry, F. H. Fenton, Minimal model for human ventricular action potentials in tissue, *Journal of theoretical biology* 253 (2008) 544–560. doi:[10.1016/j.jtbi.2008.03.029](https://doi.org/10.1016/j.jtbi.2008.03.029).
- [47] R. Doste, D. Soto-Iglesias, G. Bernardino, A. Alcaine, R. Sebastian, S. Giffard-Roisin, M. Sermesant, A. Berruezo, D. Sanchez-Quintana, O. Camara, A rule-based method to model myocardial fiber orientation in cardiac biventricular geometries with outflow tracts, *International Journal for Numerical Methods in Biomedical Engineering* 35 (2019) e3185. doi:[10.1002/cnm.3185](https://doi.org/10.1002/cnm.3185).
- [48] R. Piersanti, P. C. Africa, M. Fedele, C. Vergara, L. Dedè, A. F. Corno, A. Quarteroni, Modeling cardiac muscle fibers in ventricular and atrial electrophysiology simulations, *Computer Methods in Applied Mechanics and Engineering* 373 (2021) 113468. doi:[10.1016/j.cma.2020.113468](https://doi.org/10.1016/j.cma.2020.113468).
- [49] T. O’Hara, L. Virág, A. Varró, Y. Rudy, Simulation of the undiseased human cardiac ventricular action potential: model formulation and experimental validation, *PLoS computational biology* 7 (2011) e1002061. doi:[10.1371/journal.pcbi.1002061](https://doi.org/10.1371/journal.pcbi.1002061).
- [50] E. Passini, A. Mincholé, R. Coppini, E. Cerbai, B. Rodriguez, S. Severi, A. Bueno-Orovio, Mechanisms of pro-arrhythmic abnormalities in ventricular repolarisation and anti-arrhythmic therapies in human hypertrophic cardiomyopathy, *Journal of molecular and cellular cardiology* 96 (2016) 72–81. doi:[10.1016/j.yjmcc.2015.09.003](https://doi.org/10.1016/j.yjmcc.2015.09.003).
- [51] S. Dutta, K. C. Chang, K. A. Beattie, J. Sheng, P. N. Tran, W. W. Wu, M. Wu, D. G. Strauss, T. Colatsky, Z. Li, Optimization of an in silico cardiac cell model for proarrhythmia risk assessment, *Frontiers in Physiology* 8 (2017). doi:[10.3389/fphys.2017.00616](https://doi.org/10.3389/fphys.2017.00616).
- [52] S. Land, S.-J. Park-Holohan, N. P. Smith, C. G. Dos Remedios, J. C. Kentish, S. A. Niederer, A model of cardiac contraction based on novel measurements of tension development in human cardiomyocytes, *Journal of molecular and cellular cardiology* 106 (2017) 68–83. doi:[10.1016/j.yjmcc.2017.03.008](https://doi.org/10.1016/j.yjmcc.2017.03.008).
- [53] G. A. Holzapfel, R. W. Ogden, Constitutive modelling of passive myocardium: A structurally based framework for material characterization, *Philosophical Transactions of the Royal Society A: Mathematical, Physical and Engineering Sciences* 367 (2009) 3445–3475. doi:[10.1098/rsta.2009.0091](https://doi.org/10.1098/rsta.2009.0091).

- [54] F. Levrero-Florencio, F. Margara, E. Zacur, A. Bueno-Orovio, Z. J. Wang, A. Santiago, J. Aguado-Sierra, G. Houzeaux, V. Grau, D. Kay, M. Vázquez, R. Ruiz-Baier, B. Rodriguez, Sensitivity analysis of a strongly-coupled human-based electromechanical cardiac model: Effect of mechanical parameters on physiologically relevant biomarkers, *Computer Methods in Applied Mechanics and Engineering* 361 (2020) 112762. URL: <https://doi.org/10.1016/j.cma.2019.112762>. doi:10.1016/j.cma.2019.112762.
- [55] N. Westerhof, J. W. Lankhaar, B. E. Westerhof, The arterial windkessel, *Medical and Biological Engineering and Computing* 47 (2009) 131–141. doi:10.1007/s11517-008-0359-2.
- [56] Y. Shi, P. Lawford, R. Hose, Review of Zero-D and 1-D Models of Blood Flow in the Cardiovascular System, *BioMedical Engineering Online* 10 (2011). doi:10.1186/1475-925X-10-33.
- [57] T. Belytschko, W. K. Liu, B. Moran, K. Elkhodary, *Nonlinear finite elements for continua and structures*, John Wiley & sons, 2014.
- [58] J. Hetherington, H. Carver, R. Nash, M. O. Bernabeu, M. Mazzeo, S. Manos, hemelb-codes, <https://github.com/hemelb-codes>, 2024.
- [59] S. Succi, *The Lattice Boltzmann Equation: For Complex States of Flowing Matter*, Oxford University Press Oxford, 2018. URL: <https://academic.oup.com/book/43703>. doi:10.1093/oso/9780199592357.001.0001.
- [60] T. Krüger, H. Kusumaatmaja, A. Kuzmin, O. Shardt, S. Goncalo, E. M. Viggen, *The Lattice Boltzmann Method*, Springer Cham, 2017. URL: <https://link.springer.com/book/10.1007/978-3-319-44649-3>. doi:<https://doi.org/10.1007/978-3-319-44649-3>.
- [61] R. W. Nash, H. B. Carver, M. O. Bernabeu, J. Hetherington, D. Groen, T. Krüger, P. V. Coveney, Choice of boundary condition for lattice-Boltzmann simulation of moderate-Reynolds-number flow in complex domains, *Physical Review E - Statistical, Nonlinear, and Soft Matter Physics* 89 (2014) 1–13. doi:10.1103/PhysRevE.89.023303.
- [62] D. Groen, R. A. Richardson, R. Coy, U. D. Schiller, H. Chandrashekar, F. Robertson, P. V. Coveney, Validation of patient-specific cerebral blood flow simulation using transcranial Doppler measurements, *Frontiers in Physiology* 9 (2018) 1–13. doi:10.3389/fphys.2018.00721.
- [63] J. W. S. McCullough, P. V. Coveney, High fidelity blood flow in a patient-specific arteriovenous fistula, *Scientific Reports* 11 (2021) 1–12. URL: <https://doi.org/10.1038/s41598-021-01435-8>. doi:10.1038/s41598-021-01435-8.
- [64] R. Richardson, J. Hetherington, H. Carver, R. Nash, M. O. Bernabeu, M. Mazzeo, S. Manos, hemelb-codes/HemePure, <https://github.com/hemelb-codes/HemePure>, 2024.
- [65] P. L. Bhatnagar, E. P. Gross, M. Krook, A Model for Collision Processes in Gases. I. Small Amplitude Processes in Charged and Neutral One-Component Systems, *Physical Review* 94 (1954) 511–525. URL: <https://link.aps.org/doi/10.1103/PhysRev.94.511>. doi:10.1103/PhysRev.94.511.
- [66] N. M. Wilson, A. K. Ortiz, A. B. Johnson, The Vascular Model Repository: A Public Resource of Medical Imaging Data and Blood Flow Simulation Results, *Journal of Medical Devices* 7 (2013). URL: <https://doi.org/10.1115/1.4025983>. doi:10.1115/1.4025983.

- [67] V. Kannojiya, A. K. Das, P. K. Das, Simulation of Blood as Fluid: A Review from Rheological Aspects, *IEEE Reviews in Biomedical Engineering* 14 (2021) 327–341. doi:[10.1109/RBME.2020.3011182](https://doi.org/10.1109/RBME.2020.3011182).
- [68] B. Thomas, K. S. Sumam, Blood Flow in Human Arterial System-A Review, *Procedia Technology* 24 (2016) 339–346. URL: <https://www.sciencedirect.com/science/article/pii/S2212017316301293>. doi:<https://doi.org/10.1016/j.protcy.2016.05.045>.
- [69] M. Bouzidi, M. Firdaouss, P. Lallemand, Momentum transfer of a Boltzmann-lattice fluid with boundaries, *Physics of Fluids* 13 (2001) 3452–3459. doi:[10.1063/1.1399290](https://doi.org/10.1063/1.1399290).
- [70] S. C. Y. Lo, J. W. S. McCullough, P. V. Coveney, Parametric analysis of an efficient boundary condition to control outlet flow rates in large arterial networks, *Scientific Reports* 12 (2022) 1–12. URL: <https://doi.org/10.1038/s41598-022-21923-9>. doi:[10.1038/s41598-022-21923-9](https://doi.org/10.1038/s41598-022-21923-9).
- [71] A. J. Ladd, Numerical Simulations of Particulate Suspensions Via a Discretized Boltzmann Equation. Part 1. Theoretical Foundation, *Journal of Fluid Mechanics* 271 (1994) 285–309. doi:[10.1017/S0022112094001771](https://doi.org/10.1017/S0022112094001771).
- [72] L. Grinberg, G. E. Karniadakis, Outflow boundary conditions for arterial networks with multiple outlets, *Annals of Biomedical Engineering* 36 (2008) 1496–1514. doi:[10.1007/s10439-008-9527-7](https://doi.org/10.1007/s10439-008-9527-7).
- [73] E. Vergnault, O. Malaspinas, P. Sagaut, A lattice Boltzmann method for nonlinear disturbances around an arbitrary base flow, *Journal of Computational Physics* 231 (2012) 8070–8082. URL: <http://dx.doi.org/10.1016/j.jcp.2012.07.021>. doi:[10.1016/j.jcp.2012.07.021](https://doi.org/10.1016/j.jcp.2012.07.021).
- [74] E. Ezzatneshan, Implementation of curved wall boundary and absorbing open boundary conditions for the d3q19 lattice boltzmann method for simulation of incompressible uid ows, *Scientia Iranica* 26 (2019) 2329–2341. doi:[10.24200/sci.2018.20608](https://doi.org/10.24200/sci.2018.20608).
- [75] X. Xue, J. W. S. McCullough, S. C. Y. Lo, I. Zacharoudiou, B. Joó, P. V. Coveney, The Lattice Boltzmann Based Large Eddy Simulations for the Stenosis of the Aorta, volume 3, Springer Nature Switzerland, 2024. URL: http://dx.doi.org/10.1007/978-3-031-63775-9_30. doi:[10.1007/978-3-031-63775-9_{_}30](https://doi.org/10.1007/978-3-031-63775-9_{_}30).
- [76] Zygote, Solid 3d human heart model, <https://www.zygote.com/cad-models/solid-3d-human-anatomy/solid-3d-human-heart>, 2015.
- [77] A. Hager, H. Kaemmerer, U. Rapp-Bernhardt, S. Blücher, K. Rapp, T. M. Bernhardt, M. Galanski, J. Hess, Diameters of the thoracic aorta throughout life as measured with helical computed tomography, *Journal of Thoracic and Cardiovascular Surgery* 123 (2002) 1060–1066. doi:[10.1067/mtc.2002.122310](https://doi.org/10.1067/mtc.2002.122310).
- [78] R. Erbel, F. Alfonso, C. Boileau, O. Dirsch, B. Eber, A. Haverich, H. Rakowski, J. Struyven, K. Radegran, U. Sechtem, J. Taylor, C. Zollikofer, W. W. Klein, B. Mulder, L. A. Providencia, Diagnosis and management of aortic dissection: Recommendations of the Task Force on Aortic Dissection, *European Society of Cardiology, European Heart Journal* 22 (2001) 1642–1681. doi:[10.1053/euhj.2001.2782](https://doi.org/10.1053/euhj.2001.2782).

- [79] G. Xiong, C. A. Figueroa, N. Xiao, C. A. Taylor, Simulation of blood flow in deformable vessels using subject-specific geometry and spatially varying wall properties, *International Journal for Numerical Methods in Biomedical Engineering* 27 (2011) 1000–1016. URL: http://knowledgebase.terrafrica.org/fileadmin/user_upload/terrafrica/docs/Final_Rockefeller_Report4April08.pdf. doi:10.1002/cnm.1404.
- [80] J. W. S. McCullough, R. Richardson, UCL-CCS/HemePure_tools, https://github.com/UCL-CCS/HemePure_tools, 2024.
- [81] S. C. Y. Lo, J. W. S. McCullough, X. Xue, P. V. Coveney, Uncertainty quantification of the impact of peripheral arterial disease on abdominal aortic aneurysms in blood flow simulations, *Journal of the Royal Society Interface* 21 (2024). doi:10.1098/rsif.2023.0656.
- [82] A. Boccadifuoco, A. Mariotti, K. Capellini, S. Celi, M. V. Salvetti, Validation of Numerical Simulations of Thoracic Aorta Hemodynamics: Comparison with In Vivo Measurements and Stochastic Sensitivity Analysis, *Cardiovascular Engineering and Technology* 9 (2018) 688–706. doi:10.1007/s13239-018-00387-x.
- [83] P. Youssefi, A. Gomez, C. Arthurs, R. Sharma, M. Jahangiri, C. A. Figueroa, Impact of patient-specific inflow velocity profile on hemodynamics of the thoracic aorta, *Journal of Biomechanical Engineering* 140 (2018) 1–14. doi:10.1115/1.4037857.
- [84] S. Madhavan, E. M. Kemmerling, The effect of inlet and outlet boundary conditions in image-based CFD modeling of aortic flow, *BioMedical Engineering Online* 17 (2018) 1–20. doi:10.1186/s12938-018-0497-1.
- [85] F. U. Mattace-Raso, A. Hofman, G. C. Verwoert, J. C. Wittemana, I. Wilkinson, J. Cockcroft, C. McEniery, Yasmina, S. Laurent, P. Boutouyrie, E. Bozec, T. W. Hansen, C. Torp-Pedersen, H. Ibsen, J. Jeppesen, S. J. Vermeersch, E. Rietzschel, M. de Buyzere, T. C. Gillebert, L. van Bortel, P. Segers, C. Vlachopoulos, C. Aznaouridis, C. Stefanadis, A. Benetos, C. Labat, P. Lacolley, C. D. Stehouwer, G. Nijpels, J. M. Dekker, I. Ferreira, J. W. Twisk, S. Czernichow, P. Galan, S. Herberg, B. Pannier, A. Guérin, G. London, J. Kennedy Cruickshank, S. G. Anderson, A. Paini, E. A. Rosei, M. L. Muiasan, M. Salvetti, J. Filipovsky, J. Seidlerova, M. Dolejsova, Determinants of pulse wave velocity in healthy people and in the presence of cardiovascular risk factors: ‘Establishing normal and reference values’, *European Heart Journal* 31 (2010) 2338–2350. doi:10.1093/eurheartj/ehq165.
- [86] S. Piperno, Explicit/implicit fluid/structure staggered procedures with a structural predictor and fluid subcycling for 2D inviscid aeroelastic simulations, *International Journal for Numerical Methods in Fluids* 25 (1997) 1207–1226. doi:10.1002/(SICI)1097-0363(19971130)25:10<1207::AID-FLD616>3.0.CO;2-R.
- [87] U. Küttler, C. Förster, W. A. Wall, A solution for the incompressibility dilemma in partitioned fluid-structure interaction with pure dirichlet fluid domains, *Computational Mechanics* 38 (2006) 417–429. doi:10.1007/s00466-006-0066-5.
- [88] P. J. Kilner, G. Z. Yang, R. H. Mohiaddin, D. N. Firmin, D. B. Longmore, Helical and retrograde secondary flow patterns in the aortic arch studied by three-directional magnetic resonance velocity mapping, *Circulation* 88 (1993) 2235–2247. doi:10.1161/01.cir.88.5.2235.

- [89] J. P. Escobar Kvitting, T. Ebbers, L. Wigström, J. Engvall, C. L. Olin, A. F. Bolger, Flow patterns in the aortic root and the aorta studied with time-resolved, 3-dimensional, phase-contrast magnetic resonance imaging: Implications for aortic valve-sparing surgery, *Journal of Thoracic and Cardiovascular Surgery* 127 (2004) 1602–1607. doi:[10.1016/j.jtcvs.2003.10.042](https://doi.org/10.1016/j.jtcvs.2003.10.042).
- [90] P. Coveney, R. Highfield, *Virtual You: How Building Your Digital Twin Will Revolutionize Medicine and Change Your Life*, Princeton University Press, 2023. URL: <http://www.jstor.org/stable/10.2307/j.ctv2xqngmf>. doi:[10.2307/j.ctv2xqngmf](https://doi.org/10.2307/j.ctv2xqngmf).